Production cross sections of light and charmed mesons in e^+e^- annihilation near 10.58 GeV

R. Seidl, I. Adachi, H. Aihara, T. Aushev, R. Ayad, Sw. Banerjee, K. Belous, J. Bennett, M. Bessner,
B. Bhuyan, D. Biswas, D. Bodrov, M. Bračko, P. Branchini, T. E. Browder, A. Budano, M. Campajola,
K. Chilikin, K. Cho, S.-K. Choi, Y. Choi, S. Choudhury, S. Das, G. De Nardo, G. De Pietro, F. Di Capua,
J. Dingfelder, Z. Doležal, T. V. Dong, D. Dossett, P. Ecker, T. Ferber, B. G. Fulsom, V. Gaur, A. Giri,
P. Goldenzweig, E. Graziani, Y. Guan, K. Gudkova, C. Hadjivasiliou, T. Hara, H. Hayashii, D. Herrmann,
W.-S. Hou, C.-L. Hsu, K. Inami, N. Ipsita, A. Ishikawa, R. Itoh, M. Iwasaki, W. W. Jacobs, S. Jia, Y. Jin,
K. K. Joo, A. B. Kaliyar, C. Kiesling, C. H. Kim, D. Y. Kim, K.-H. Kim, P. Kodyš, A. Korobov, S. Korpar,
P. Križan, P. Krokovny, D. Kumar, K. Kumara, Y.-J. Kwon, T. Lam, L. K. Li, Y. B. Li, L. Li Gioi,
J. Libby, D. Liventsev, Y. Ma, M. Masuda, T. Matsuda, D. Matvienko, M. Merola, K. Miyabayashi,
R. Mussa, M. Nakao, A. Natochii, M. Niiyama, S. Nishida, S. Ogawa, H. Ono, G. Pakhlova, S. Pardi,
J. Park, S.-H. Park, A. Passeri, S. Patra, S. Paul, T. K. Pedlar, R. Pestotnik, L. E. Piilonen, T. Podobnik,
E. Prencipe, M. T. Prim, G. Russo, S. Sandilya, L. Santelj, V. Savinov, G. Schnell, C. Schwanda, Y. Seino,
K. Senyo, M. E. Sevior, W. Shan, J.-G. Shiu, B. Shwartz, J. B. Singh, E. Solovieva, M. Starič,
M. Sumihama, M. Takizawa, K. Tanida, F. Tenchini, T. Uglov, Y. Unno, S. Uno, Y. Usov, C. Van Hulse,
A. Vinokurova, A. Vossen, M.-Z. Wang, B. D. Yabsley, W. Yan, Y. Yook, C. Z. Yuan, L. Yuan,
Z. P. Zhang, and V. Zhilich

(Belle Collaboration)

We report measurements of production cross sections for ρ^+, ρ^0, ω, K^{*+}, K^{*0}, ϕ, η, K_S^0, $f_0(980)$, D^+, D^0, D_s^+, D^{*+}, D^{*0}, and D_s^{*+} in e^+e^- collisions at a center-of-mass energy near 10.58 GeV. The data were recorded by the Belle experiment, consisting of 571 fb^{-1} at 10.58 GeV and 74 fb^{-1} at 10.52 GeV. Production cross sections are extracted as a function of the fractional hadron momentum x_p. The measurements are compared to PYTHIA Monte Carlo generator predictions with various fragmentation settings, including those that have increased fragmentation into vector mesons over pseudoscalar mesons. The cross sections measured for light hadrons are consistent with no additional increase of vector over pseudoscalar mesons. The charmed-meson cross sections are compared to earlier measurements—when available—including older Belle results, which they supersede. They are in agreement before application of an improved initial-state radiation correction procedure that causes slight changes in their x_p shapes.

I. INTRODUCTION

Fragmentation functions (FFs) describe the formation of hadrons, states of confined quarks and gluons (collectively denoted partons), out of asymptotically free, highly energetic partons. As they cannot be calculated from first principles in quantum chromodynamics they need to be extracted experimentally. These nonperturbative objects in turn can be used to describe hadron-production cross sections in various high-energy processes since the nonperturbative fragmentation functions (and potentially other nonperturbative objects, like parton distribution functions) factorize from the calculable hard interactions [1]. High-precision knowledge of FFs can thus provide additional sensitivity to the flavor, spin, and transverse momentum of partons, e.g., in measurements of parton distributions and therefore to the three-dimensional and spin-structure of the nucleon, one of the key scientific goals of the future electron-ion collider (EIC) [2,3]. Given that in electron-positron annihilation no hadrons exist in the initial state, such collisions are well suited for obtaining fragmentation functions as they are the only nonperturbative functions that need to be modeled.

So far, many measurements have been performed at various collision energies for light and charmed hadron

production [4–16]. What has not been studied intensively to date are fragmentation functions for the various vector mesons (VMs) [17,18], even though they have recently gained increased interest. Given their slightly higher masses compared to their pseudoscalar counterparts, the production cross sections might be reduced at low energies, but in high-energy processes no *a priori* reason exists that suggests they would be suppressed. Many Monte Carlo (MC) generators such as PYTHIA [19,20] treat the fragmentation of light partons into pseudoscalar and vector mesons equally apart from their mass dependence.

Understanding the production of VMs can address various open questions. For example, the muon puzzle [21] in modeling ultra-high-energetic cosmic-ray air-shower measurements can be related to the relative strength of the production of neutral rho mesons vs neutral pions as it affects the hadronic-shower evolution [22,23], and thus the muon content of the cosmic-ray air shower. Similarly, while strong decays are explicitly included in the formal description of FFs, the decay contributions to pion and kaon FFs may exhibit significantly different transverse-momentum dependencies as compared, e.g., to the contributions from directly produced pions and kaons, particularly at low momenta. Last, the transverse-spin dependent Collins FFs [24] are expected to behave differently for VMs than for pseudoscalar mesons in various models [25–27], due to the way the polarized quark has to combine in the fragmentation process to create either a spin-zero or spin-one meson. While few measurements related to VM Collins asymmetries exist [28], the measurements presented here will provide the unpolarized baseline for such studies.

Additionally, we present an update of D-meson cross sections as a function of the fractional hadron momentum that confirm and supersede previous Belle measurements [12] and that are also compared to other published results. Furthermore, D_s^{*+} meson cross sections are presented for the first time. The formation of heavy-flavor mesons is of general interest at high-energy colliders and particularly in heavy-ion collisions, where the formation of heavy-flavor mesons may be modified by the nuclear environment or the quark-gluon plasma. At the EIC, D mesons in the final state will be prime candidates to single out gluonic hard interactions and thus help to access the gluon (spin and momentum) structure of the nucleon [3].

Last, also the cross sections for several other light pseudoscalar mesons are reported since those are produced in abundance in high-energy processes and provide complementary sensitivity, particularly to strange quarks even in experimental setups where charged kaons cannot be directly identified.

The measurements reported here will help improve the precision of FF extractions that are needed as input in all of these mentioned processes. Since the high precision of recent Belle fragmentation-related measurements [29] has challenged the flexibility of various global fragmentation

fits, we provide (online) all sources of uncertainties separately, together with the information on whether they are global scale uncertainties, correlated among bins or uncorrelated.

This paper is organized as follows. After this introduction, in Sec. II, the datasets and MC simulations are discussed. Section III details the event and particle selection. In Sec. IV, the invariant-mass fits and the subsequent acceptance and efficiency corrections are described. Section V covers all systematic consistency tests and summarizes the total systematic uncertainty budgets of these measurements, before the final results are presented in Sec. VI and summarized in Sec. VII.

II. DATASETS AND MONTE CARLO SIMULATIONS

The data were taken with the Belle detector [30,31] at the asymmetric electron-positron collider KEKB [32,33]. Here, 8 GeV electrons collided with 3.5 GeV positrons at the center-of-mass energy of the $\Upsilon(4S)$ resonance at 10.58 GeV (denoted on-resonance throughout this manuscript). We also take data at 60 MeV below the $\Upsilon(4S)$ resonance (denoted as continuum). In addition to the open quark-antiquark pair production (at leading order) and other QED processes, the on-resonance data also contain events from $\Upsilon(4S)$ production with their subsequent decays into B-meson pairs. The accumulated datasets consist of 558 fb^{-1} in the on-resonance sample and 74 fb^{-1} in the continuum sample. The two samples are initially analyzed separately in order to compare the results for consistency and to see the contribution of B decays to the cross sections.

The events were collected with the Belle detector, which is a large-solid-angle magnetic spectrometer comprising of a silicon vertex detector (SVD), a 50-layer central drift chamber, an array of aerogel threshold Cherenkov counters (ACC), a barrel-like arrangement of time-of-flight (TOF) scintillation counters, and an electromagnetic calorimeter (ECL) made of CsI(Tl) crystals located inside a superconducting solenoid coil that provides a 1.5 T magnetic field. An iron flux-return located outside of the coil is instrumented to detect K_L^0 mesons and to identify muons (KLM). The detector is described in detail in publications [30,31]. The data for this measurement were collected in a detector configuration consisting of a beampipe with a 1.5 cm radius and 1 mm thickness, a 4-layer SVD, and a small-cell inner drift chamber.

For simulations, PYTHIA6 [34] was used as a generator for the $e^+e^- \rightarrow q\bar{q}$ events, where q is a u, d, s, or c quark (denoted as udsc MC and specified as the *old Belle tune* in the data-MC comparisons), as well as other QED processes. This generator is included in the package EvtGen [35], which also handles the $\Upsilon(4S)$ production and the subsequent decays. Additionally, dedicated τ-pair simulations were obtained using the generator KKMC [36] and the TAUOLA package [37]. All generated events were fed into full

TABLE I.   Parameters for the various tunes used in the comparison to the measured cross sections reported here. Each row corresponds to a PYTHIA/JetSet setting that differs for at least one of the tunes. Empty entries indicate the default setting. The tune labeled "High VM" has an increased fraction of light quarks fragmenting into vector over pseudoscalar mesons compared to the default setting. A brief explanation of each parameter is also given; for details see Ref. [19]. The central values for the acceptance and ISR corrections were based on the Belle tune.

	PYTHIA default	Belle	ALEPH	LEP/ Tevatron	HERMES	Old Belle	High VM	Explanation
PARJ(1)	0.1		0.106	0.073	0.029			Diquark suppression
PARJ(2)	0.3		0.285	0.2	0.283			Strange suppression
PARJ(3)	0.4		0.71	0.94	1.2			Strange diquark suppression
PARJ(4)	0.05			0.032				Spin 1 diquark suppression
PARJ(11)	0.5		0.55	0.31			0.6	Light quark spin 1 meson probability
PARJ(12)	0.6		0.47	0.4				Strange quark spin 1 meson probability
PARJ(13)	0.75		0.65	0.54				Heavy quark spin 1 meson probability
PARJ(14)	0		0.02			0.05	0.05	S 0, L 1, J 1
PARJ(15)	0		0.04			0.05	0.05	S 1, L 1 J 0
PARJ(16)	0		0.02			0.05	0.05	S 1, L 1 J 1
PARJ(17)	0		0.2			0.05	0.05	S 1, L 1 J 2
PARJ(19)	1		0.57					Extra baryon suppression
PARJ(21)	0.36		0.37	0.325	0.4	0.28		p_x, p_y
PARJ(25)	1			0.63		0.27		η suppression
PARJ(26)	0.4		0.27	0.12				η' suppression
PARJ(33)	0.8				0.3			End of fragmentation energy
PARJ(41)	0.3		0.4	0.5	1.94	0.32		Lund parameter a
PARJ(42)	0.58		0.796	0.6	0.544	0.62		Lund parameter b
PARJ(45)	0.5				1.05			a factor for diquarks
PARJ(47)	1.0			0.67				Heavy quark endpoint modification
PARJ(54)	−0.050	−0.04	−0.04					Charm FF parameterization
PARJ(55)	−0.005	−0.004	−0.0035					Bottom FF parameterization
PARJ(81)	0.29		0.292	0.29				Λ value in running α_s
PARJ(82)	1.0		1.57	1.65				Mass cut-off for parton showers
MSTJ(11)	4		3	5		4		Type of FF model
MSTJ(12)	2		3		1			Baryon production model
MSTJ(26)	2	0				0		B-$\bar{B}$ mixing
MSTJ(45)	5				4			Max. flavor in gluon shower
MSTJ(107)	0	1				1		Radiative corrections

Geant3 [38] detector simulations and the event reconstruction for further analysis. For the quark-pair production events, which are the main source for the FF information this analysis provides, additional events were generated with various fragmentation parameter settings in PYTHIA, hereafter denoted as tunes (see Table I). The latter events provide a tool to evaluate the systematic effects of these tunes on acceptance and initial-state radiation corrections, as well as provide information regarding the most suitable fragmentation settings for the generator. All simulations are performed at $\sqrt{s} = 10.58$ GeV as the difference in center-of-mass energies has a negligible effect on all correction steps.

III. EVENT AND PARTICLE SELECTION CRITERIA

Hadronic events are selected with a visible-energy requirement of at least 7 GeV, obtained from the sum of the momenta of reconstructed tracks and energies of trackless calorimeter clusters, in order to reduce the contamination from $e^+e^- \to \tau^+\tau^-$ events. The heavy-jet mass is defined as the greater of the invariant mass sums of all particles in one hemisphere as generated by the plane perpendicular to the thrust axis [39]. It is required that the heavy-jet mass lies above 1.8 GeV or that the ratio of the heavy-jet mass to the visible energy lies above 0.25. These criteria reduce the amount of two-photon processes. Additionally, at least three charged tracks have to be reconstructed, which also reduces the contamination of two-photon processes, as well as lepton-pair production.

A charged particle is selected if the track emerges from a region that is less than 4 cm away from the nominal interaction point along the positron beam direction and less than 2 cm away perpendicularly (except for K_S^0 candidates). Tracks considered also need to be reconstructed in the barrel region of the detector where $-0.511 < \cos\theta_{Lab} < 0.842$,

and information on particle identification is available from all relevant detectors that contribute to its determination. A minimum transverse momentum of 50 MeV [40] is required to ensure the tracks traverse all particle identification (PID) detectors. The information from the ACC, TOF, drift chamber, ECL, and KLM is then used to identify the particles using likelihood ratios between pion, kaon, and proton hypotheses, as well as muon or electron likelihoods. Particle misidentification is corrected as described in Ref. [11] using a predominantly data-based calibration of the above five particle types in a fine 17×9 laboratory-momentum and polar-angular binning. For momenta below 500 MeV, the particle type given by the PID detectors is assumed to be correct as the flight times are sufficiently long. In regions where the phase space requires particles with these lower laboratory momenta (to be discussed in further detail below), such particles are also considered but require an additional reconstruction efficiency correction. This predominantly affects the slow charged pion of the $D^{*+} \to D^0 \pi^+$ decay, as well as the region of low fractional momentum for a few of the mesons considered here.

Neutral-pion candidates are selected by the electromagnetic calorimeters if the invariant mass of a pair of trackless clusters falls between 120 and 150 MeV, which is more than approximately 2 standard deviations on the diphoton mass peak at Belle. Also a minimum transverse momentum of 50 MeV is required for each of the candidate photons in order to reduce the combinatorial background. Despite the larger acceptance of the calorimeter, for most reconstructed pions the same acceptance and momentum requirements as for charged hadrons are applied for consistency reasons, with the same exception for the slow pion of the $D^{*0} \to D^0 \pi^0$ decay and other final states where the phase space requires slow pions.

Once the produced particles are identified, they are organized into either pairs or triplets for the decay channels $\rho^0 \to \pi^+ \pi^-$, $\rho^\pm \to \pi^\pm \pi^0$, $\omega \to \pi^+ \pi^- \pi^0$, $K^{*0} \to K^+ \pi^-$, $K^{*\pm} \to K^\pm \pi^0$, $\phi \to K^+ K^-$, as well as for the $K^0_S \to \pi^+ \pi^-$, $\eta \to \pi^+ \pi^- \pi^0$, and $f_0(980) \to \pi^+ \pi^-$ channels. Apart from the ρ mesons, charge-conjugate states are combined and are implicitly analyzed together. For K^0_S decay candidates, the transverse decay vertex position as obtained from an additional vertex fit within 30 MeV of the nominal K^0_S mass has to be less than 5 cm away to account for the finite lifetime of this particle. For the D mesons, the following decay channels are analyzed: $D^0 \to K^- \pi^+$, $D^+ \to K^- \pi^+ \pi^+$, $D^{*+} \to D^0 \pi^+ \to (K^- \pi^+) \pi^+$, $D^{*0} \to D^0 \pi^0 \to (K^- \pi^+) \pi^0$, $D^+_s \to \phi \pi^+ \to (K^+ K^-) \pi^+$, and $D^{*+}_s \to \phi \pi^+ \gamma \to (K^+ K^-) \pi^+ \gamma$. Additional D^0 and D_s final states are also considered, but only used for consistency tests. For the D^*_s final state, the decay photon is required to be recorded as a trackless cluster with a minimum transverse momentum of 50 MeV.

The various final states are binned in 40 equidistant bins of $x_p = p_h / p_{\max}$, which is the fractional hadron momentum that takes into account the maximal momentum available for a particle of a certain mass, $p_{\max} = \sqrt{s/4 - m_h^2}$, where $\sqrt{s}$ is the total center-of-mass energy and m_h is the nominal hadron mass taken from the particle data group (PDG) [41]. Unlike the hadron fractional energy z (defined with respect to half the center-of-mass energy) that is often used for fragmentation functions, x_p is a true scaling variable that runs from zero to unity. For very low masses or very high center-of-mass energies, the two definitions are nearly identical, but for B factory energies they are substantially different. The PDG masses have been used to calculate $p_{\max}$ (and therefore x_p) also in the case of the wider resonances for which the invariant mass of the decay particles can significantly differ from the nominal mass of the parent. It is found that the differences in x_p even for the wide resonances are insignificant relative to the bin widths.

IV. SIGNAL YIELDS AND CORRECTIONS

A. Invariant-mass fits

In each x_p bin, the invariant mass of the various mesons under study is calculated in 100 mass bins that cover between ± 50 MeV and ± 220 MeV around the nominal PDG values, depending on the width of the resonance. For the two D^* states, the mass differences between D^* and D^0 are binned instead because of the small momentum of the slow pion. For intermediate particles such as the $D^0 \to K\pi$ from the D^* decays or the $\phi \to KK$ from the D_s decays, an additional mass window of 15 MeV and 7 MeV was applied, respectively, which corresponds to between 1 and 2 standard deviations of the mass peaks.

To obtain the signal yields, varying signal and background functions are fitted to the invariant-mass distributions for each final state and in each x_p bin. The functional forms for the background are chosen for most resonances to be first- to third-order polynomials that best describe the background in the MC in terms of χ^2 per degree of freedom. For the D^* and ϕ backgrounds, a threshold function of the form $[A + B(m - m_0)]^{[C+D(m-m_0)]}$ is used, where m_0 is the threshold value, and A, B, C, as well as D are free parameters.

The signal functions are either relativistic Breit-Wigner or Gaussian shapes, where again the functional form is determined by the MC signal distributions. Generally, magnitude, mass, and width are not constrained. In the actual fits to the data, the best parameters of the MC-based signal and background fits are used as initial parameters but are generally allowed to vary freely, since the absolute level of background is not perfectly described by the MC simulations in all x_p bins, as already observed in, e.g., Ref. [42]. The central mass of the signal and its width can be constrained based on MC, but that does not generally

impact the result of the fits. Such constraints can be modestly helpful in the very low x_p region for fits with large background.

In the case of neutral ρ mesons, the interference with the $\omega \to \pi\pi$ decay as well as with the nonresonant two-pion background needs to be taken into account [43,44]. Here, the fit function is

$$\frac{dN^{\pi\pi}}{dm_{\pi\pi}} = \left| A \frac{\sqrt{m_{\pi\pi} m_\rho \Gamma_\rho}}{m_{\pi\pi}^2 - m_\rho^2 + im_\rho\Gamma_\rho} + B \right.$$
$$\left. + Ce^{i\phi} \frac{\sqrt{m_{\pi\pi} m_\omega \Gamma_\omega}}{m_{\pi\pi}^2 - m_\omega^2 + im_\omega\Gamma_\omega} \right|^2, \quad (1)$$

with Breit-Wigner forms for the two resonances and a constant for the non-resonant part. The widths $\Gamma_{\rho,\omega}$ are defined by

$$\Gamma_\rho = \Gamma_\rho^0 \frac{m_\rho}{m_{\pi\pi}} \left(\frac{m_{\pi\pi}^2 - 4m_\pi^2}{m_\rho^2 - 4m_\pi^2} \right)^{3/2} \quad (2)$$

$$\Gamma_\omega = \Gamma_\omega^0 \frac{m_\omega}{m_{\pi\pi}} \left(\frac{m_{\pi\pi}^2 - 4m_\pi^2}{m_\omega^2 - 4m_\pi^2} \right)^{3/2}. \quad (3)$$

All three amplitudes A, B, and C, the $\rho - \omega$ interference phase ϕ, as well as the masses and widths of the ρ and ω are used as parameters, in addition to the background. Similarly, for charged ρ and K^*, a potential interference with a nonresonant background was included in the fit functions. Its impact on the signal is marginal but it does improve the overall quality of the fit.

The fit procedure outlined above can generally describe the data very well, as shown in Fig. 1 for an example x_p bin and all final-state particles considered here. In general, the level of background decreases with increasing x_p and is also smaller the heavier the meson considered. For all particles that contain a neutral pion as a decay product, the background level is generally higher due to the additional background in the π^0 reconstruction coming from pairs of uncorrelated photons. We also note that because D meson FFs peak at large x_p, their signal contributions can be
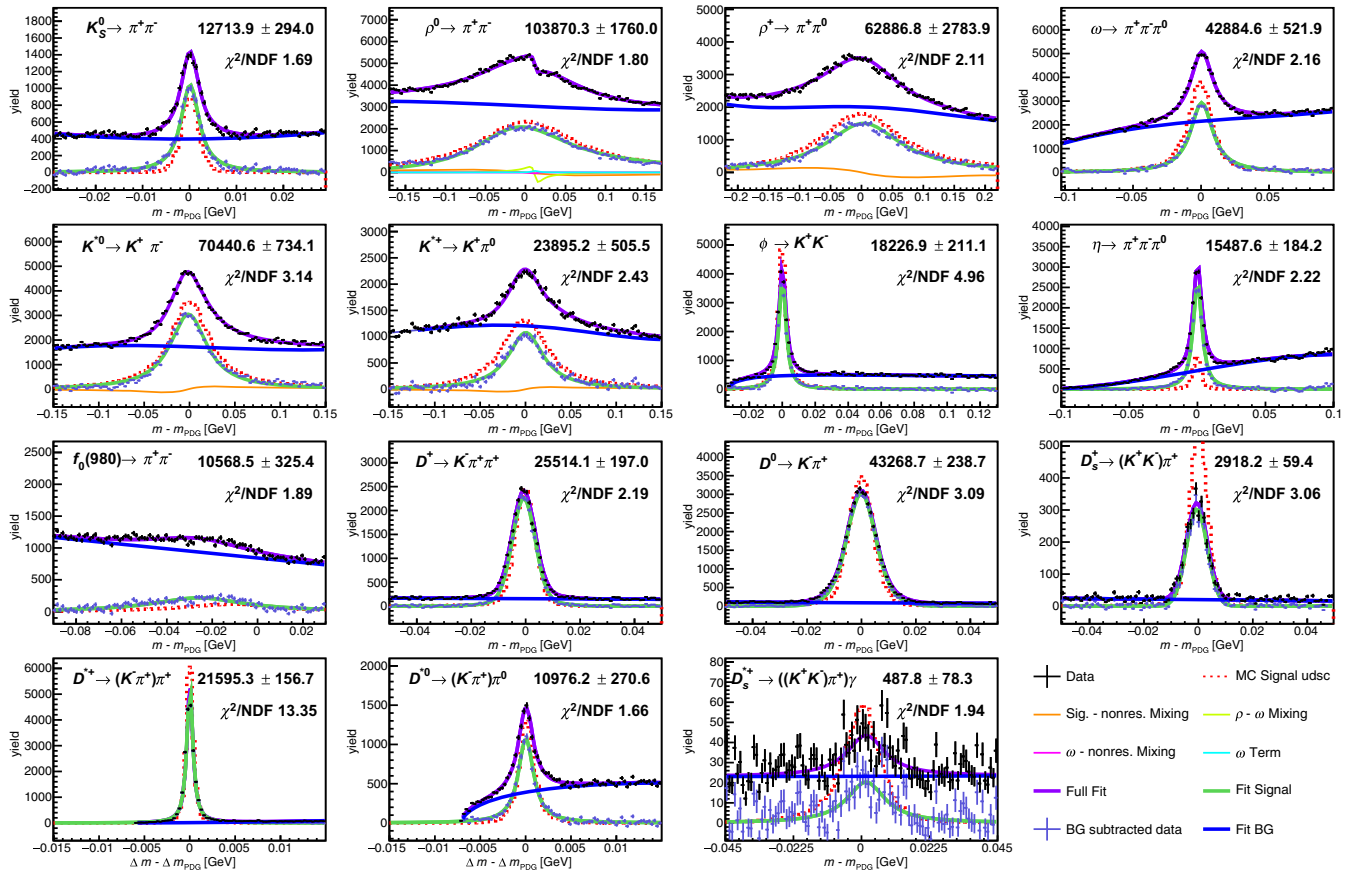

FIG. 1. Examples of the invariant-mass fits for an intermediate x_p bin (0.625–0.650) for all decay channels considered. In addition to the continuum data (black points), also the background subtracted data (blue points) and MC signal histograms (red, dashed lines) are displayed. The total fit results are shown as violet lines, while the signal parts are displayed in green and the background parts in blue. Where interference terms are considered, they are also displayed (signal to nonresonant background in orange, ω to nonresonance background in magenta, ρ-ω mixing in light green, and ω signal in cyan lines). Each panel also displays the signal yield N_{Fit} as well as the fit quality over the whole mass range used.

relatively small at low x_p, leading to large uncertainties in the extracted values.

To estimate the reliability of the signal yields thus obtained, several ways to extract the signal are considered. In addition to calculating the yield from the integral over the signal part of the fit function, also the integral of the histogram after subtracting the fitted background parameterization is calculated. The background functional form is varied to gauge the sensitivity to the background by using those fits that describe the MC background second and third-best as indicated by the reduced χ^2. These variations are all considered as sources of systematic uncertainty related to the signal extraction.

In the next step, the extracted yields N_{Fit} are corrected for the branching fractions based on the PDG [41] values, tabulated in Table II for reference. In the case of the K^* decays, the fraction decaying into $K^0\pi$ rather than the charged-kaon related final states studied here are corrected in the following acceptance-correction step because the PDG does not separate the two decay modes (hence our correction uses the MC-based branching fractions). Similarly, contributions from tails of the very wide resonances that exceed the mass windows used for the fits, most notably the ρ mesons, are also dealt with during the acceptance correction step.

Before proceeding further to the acceptance corrections that follow, the non-$q\bar{q}$ contributions, estimated from MC calculation, are subtracted from the signal yields in the final step of this stage. These contributions were obtained using the aforementioned two-photon and $e^+e^- \to \tau^+\tau^-$ MC events analyzed in the same way as the data but using the true signal contributions instead of fits, except for final states including neutral pions where the true pion association was not always available.

B. Acceptance and efficiency correction

The x_p binning chosen for this analysis is much coarser than the x_p resolution (below 0.002 for all final states and x_p bins), suggesting that no additional momentum unfolding is needed. Hence, the extracted signal yields are next corrected for detector acceptance and reconstruction efficiency. In the first step, the reconstruction within the barrel region is addressed, where for each studied final-state particle the extracted signal yields in the MC are compared to the true signal yields in the generated MC, still within the kinematic region of the barrel acceptance. In the generated MC, the vertex requirements are dropped. At this stage, also any remaining selection requirements such as the visible-energy, heavy-jet mass, track-multiplicity, and minimum momentum constraints are lifted. As can be seen in Fig. 2, the efficiencies are generally flat or slightly increasing for intermediate x_p but tend to drop towards lower x_p as well as at x_p close to one. A notable exception is the K_S^0 for which the efficiencies decrease monotonically with x_p. This is driven by the vertex requirement, which for long-lived particles becomes more stringent with increasing momentum and thus average laboratory flight distance. Closely related, a lower track reconstruction efficiency for more displaced tracks can also contribute to this behavior. The efficiencies for the different methods of extracting the signal yields are shown as well. They are very similar

TABLE II.   Branching fractions for the various decay modes of particles analyzed and reported here [41]. The branching fraction of the $f_0(980)$ is currently unknown and is assumed to be 52% as implemented in the Belle MC. The Clebsch-Gordan coefficients for the K^* decays into charged kaons are treated in the acceptance correction, as mentioned in the text.

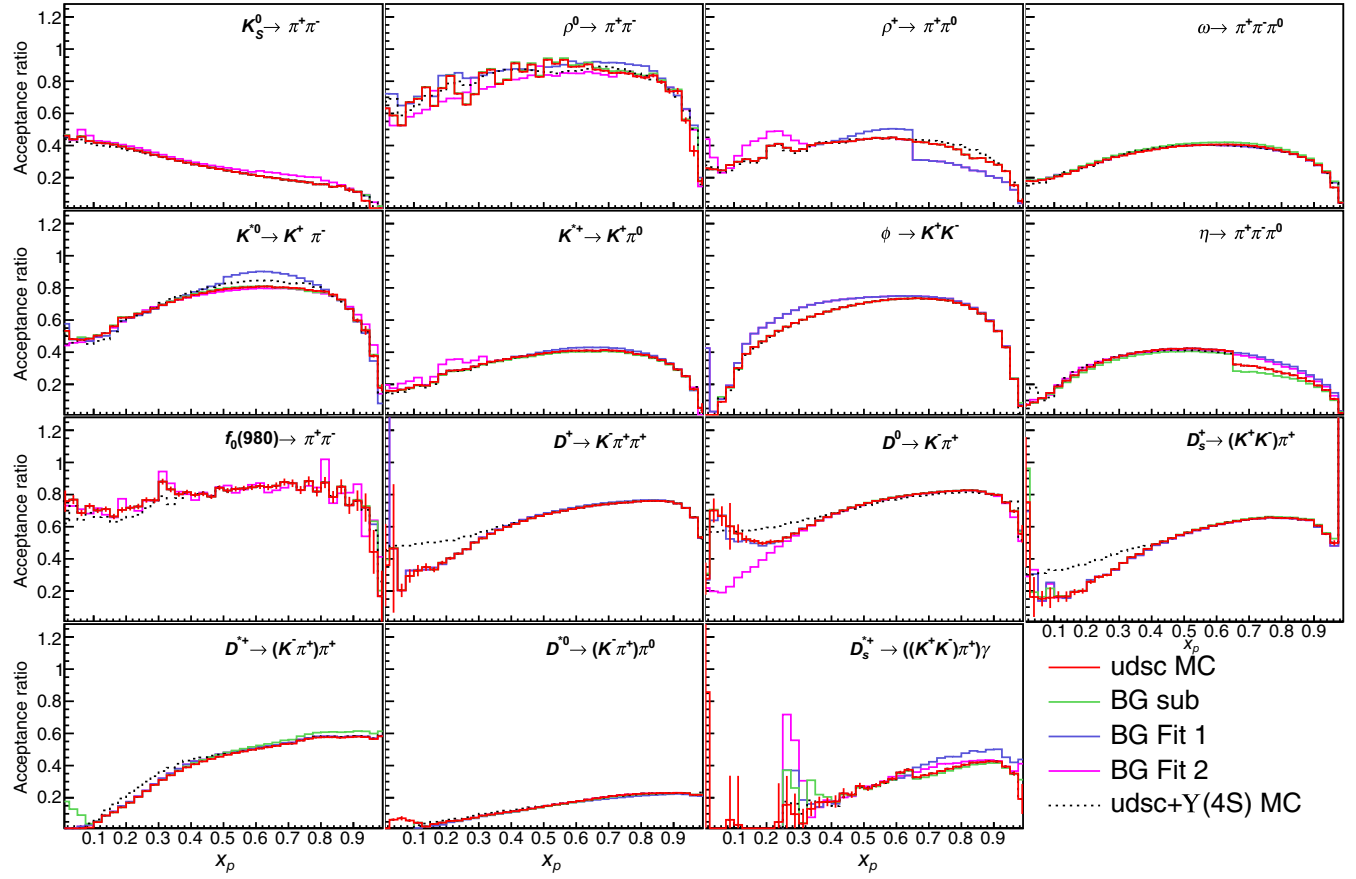| Particle	Particle decay	Branching fractions
K_S^0	$\pi^+\pi^-$	0.6920 ± 0.0005
ρ^0	$\pi^+\pi^-$	1.0 ± 0
$\rho^\pm$	$\pi^\pm\pi^0 \to \pi^\pm(\gamma\gamma)$	$(1.0) \times 0.98823$
$f_0(980)$	$\pi^+\pi^-$	0.52
K^{*0}	πK	0.99754 ± 0.00021
K^{*+}	πK	0.99902 ± 0.00009
D^0	π^+K^-	0.03947 ± 0.0003
ϕ	K^+K^-	0.491 ± 0.005
η	$\pi^+\pi^-\pi^0 \to \pi^+\pi^-(\gamma\gamma)$	$(0.2302 \pm 0.0025) \times 0.98823$
ω	$\pi^+\pi^-\pi^0 \to \pi^+\pi^-(\gamma\gamma)$	$(0.892 \pm 0.007) \times 0.98823$
D^+	$K^-\pi^+\pi^+$	0.0938 ± 0.0016
D_s^+	$\phi\pi^+ \to (K^+K^-)\pi^+$	0.0221 ± 0.0006
D_s^{*+}	$\phi\pi^+\gamma \to (K^+K^-)\pi^+\gamma$	$(0.936 \pm 0.007) \times (0.0221 \pm 0.0006)$
D^{*+}	$D^0\pi^+ \to (K^-\pi^+)\pi^+$	$(0.677 \pm 0.005) \times 0.03947$
D^{*0}	$D^0\pi^0 \to (K^-\pi^+)(\gamma\gamma)$	$(0.647 \pm 0.009) \times 0.03947 \times 0.98823$

FIG. 2.   Acceptance and reconstruction efficiencies within the barrel part of the detector as a function of x_p for the various particles considered. The differently colored points show results from the various methods of extracting the signal yields (labeled BG sub for the method of just subtracting the background function, and BG fit 1/2, for the two additional functional forms, considered) from the invariant-mass distributions, based on the quality of the MC fits for different functional forms. Those are used correspondingly in correcting their respective yields. The dashed black lines correspond to the efficiencies obtained in MC data samples including $\Upsilon(4S)$ decays.

overall, but can differ at times due to the flexibility of the background functions. They are treated separately in order to account for possible systematic under- or overestimations due to the functional forms used for the background. The efficiencies from the MC sample that additionally includes $\Upsilon(4S)$ decays are also shown for comparison. At higher x_p, which cannot be reached in $\Upsilon(4S)$ decays, the efficiencies are the same. At low x_p, where the $\Upsilon(4S)$ decays dominate, higher efficiencies are seen, particularly for the D mesons. These differences originate from the different polar-angular distributions of the original particles. D mesons from charm-pair production still follow the $1 + \cos^2\theta$ behavior of fermionic two-to-two processes (where θ is the polar angle in the center-of-mass system), while the $\Upsilon(4S)$ resonance is produced at rest and the subsequent decays into charmed mesons result in a distribution that is flat with respect to $\cos\theta$, or even maximal at central angles. For D^* mesons these differences are not quite as visible. For the lighter particles, any similar differences are hardly discernible.

In the second step of the acceptance correction, the generated MC yields within the barrel part of the detector are compared to the generated yields with 4π acceptance. The efficiencies due to the tails of the very wide resonances are also addressed in this correction step. The corrections for branching ratios of K^* decays into the charged kaons and a pion, which are the ones considered in this analysis, are handled here via the MC (although those are effectively just the isospin Clebsch-Gordan coefficients for decays into the charged and neutral kaon final-state combinations).

The extrapolation to 4π acceptance does depend on the shape of the fragmentation functions, via its implicit polar angular dependence and transverse momentum generation, introducing a tune dependence. Therefore, various MC tunes are used to compare their impact on the acceptance correction. As can be seen in Fig. 3, the efficiencies for nearly all tunes are within a few percent of each other. These variations are considered as a correlated systematic uncertainty. The only tune that deviates significantly is the HERMES tune, which has failed to describe any of the recent
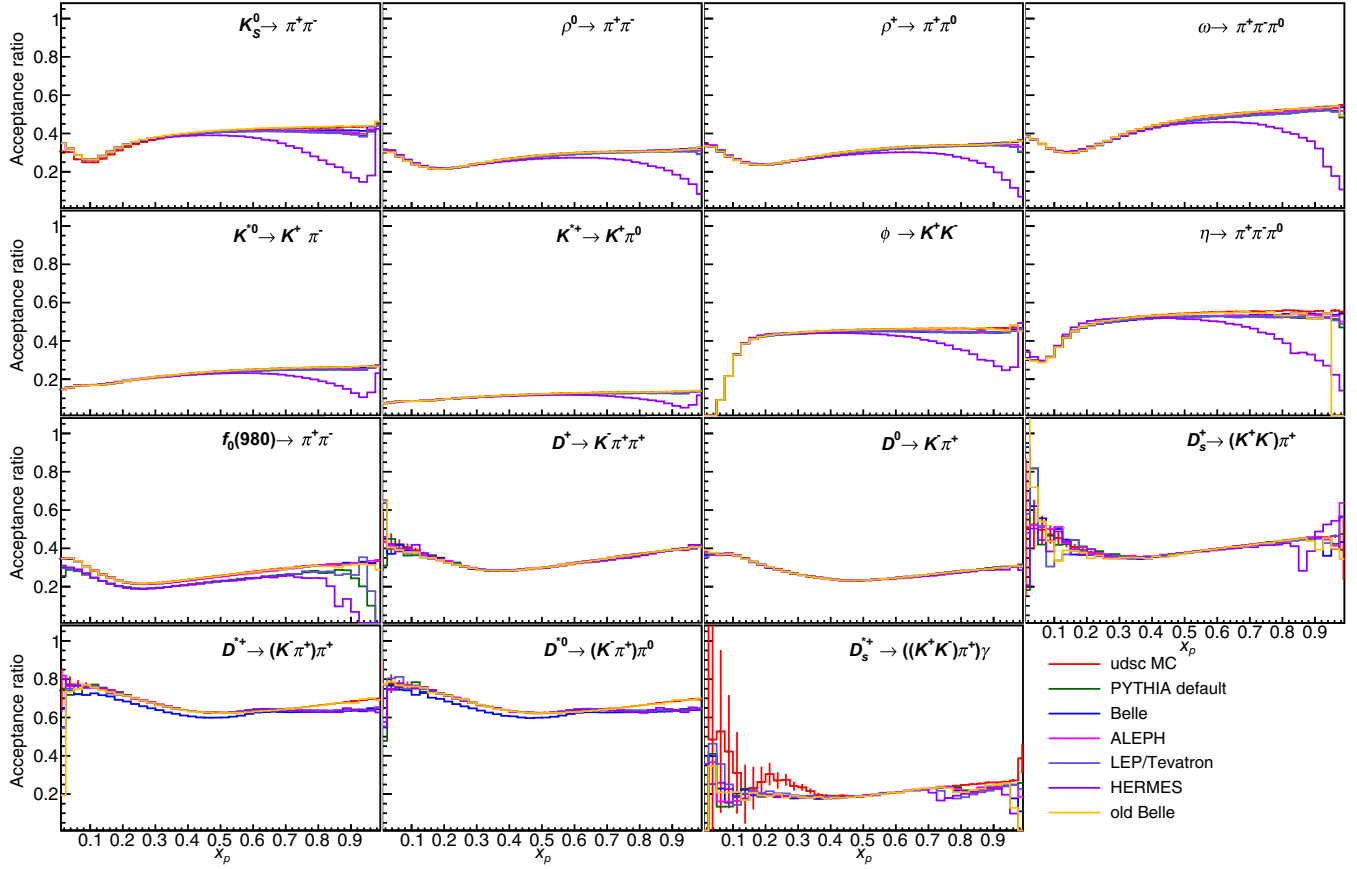
FIG. 3. Acceptance efficiencies from the full acceptance to the barrel part of the Belle detector as a function of x_p for the different particles analyzed. The colored lines show the results from the various PYTHIA tunes (using udsc samples) described in the text that are used to evaluate the tune-dependent systematic uncertainties.

Belle related fragmentation measurements and is thus not considered for inclusion in the systematic uncertainties.

In the discussion of reconstruction efficiencies, low-momentum particles require special attention. For laboratory momenta of the decay hadrons below 500 MeV, the reconstruction efficiencies are found to be overestimated in the Belle MC, e.g., from comparisons of meson cross sections that included in the analysis chain low-momentum decay particles or not. For the mesons that have a large enough phase space for their decay particles to result in sufficient yields in the two cases of including or excluding low-momentum particles, the comparison can be used to find the optimal low-momentum reconstruction efficiency. Three functional forms of the decay particles' laboratory momenta are considered for the additional low-momentum efficiency correction, together with their relative contributions for each x_p bin. A quadratic form provides the best agreement and is thus assigned as the default correction. The variations around the best functional form, as well as the other parameterizations are assigned as additional systematic uncertainties in this analysis. Due to this additional increase in systematic uncertainties, the low-momentum particle selection is only used when required by

phase space. Consequently, for lighter hadrons this selection is applied for $x_p < 0.25$ (0.35) for final states of two (three) particles. For regular D mesons and D_s, the high-momentum selection is sufficient, but for D^* the low-momentum selection is needed for x_p below 0.9 due to the small mass difference between the D^* and the D^0.

C. ISR correction

Similar to other recent Belle fragmentation measurements, the impact of initial-state photon radiation (ISR) is addressed by comparing generated MC signal yields including ISR to those where it is switched off. As the ISR photon takes away energy from the quark-antiquark system, the phase space for high-x_p hadron production (relative to the nominally available maximum momentum) gets reduced and the ratio between no-ISR and ISR becomes larger than unity. By contrast, the fraction of low-x_p hadrons increases and hence the ratio here becomes smaller than unity. This effect appears to become more prominent for the heavier particles. For lighter mesons, the ISR ratios vary only up to 10% around unity, while for D mesons, the ratios fall as low as 0.4 at low x_p and reach
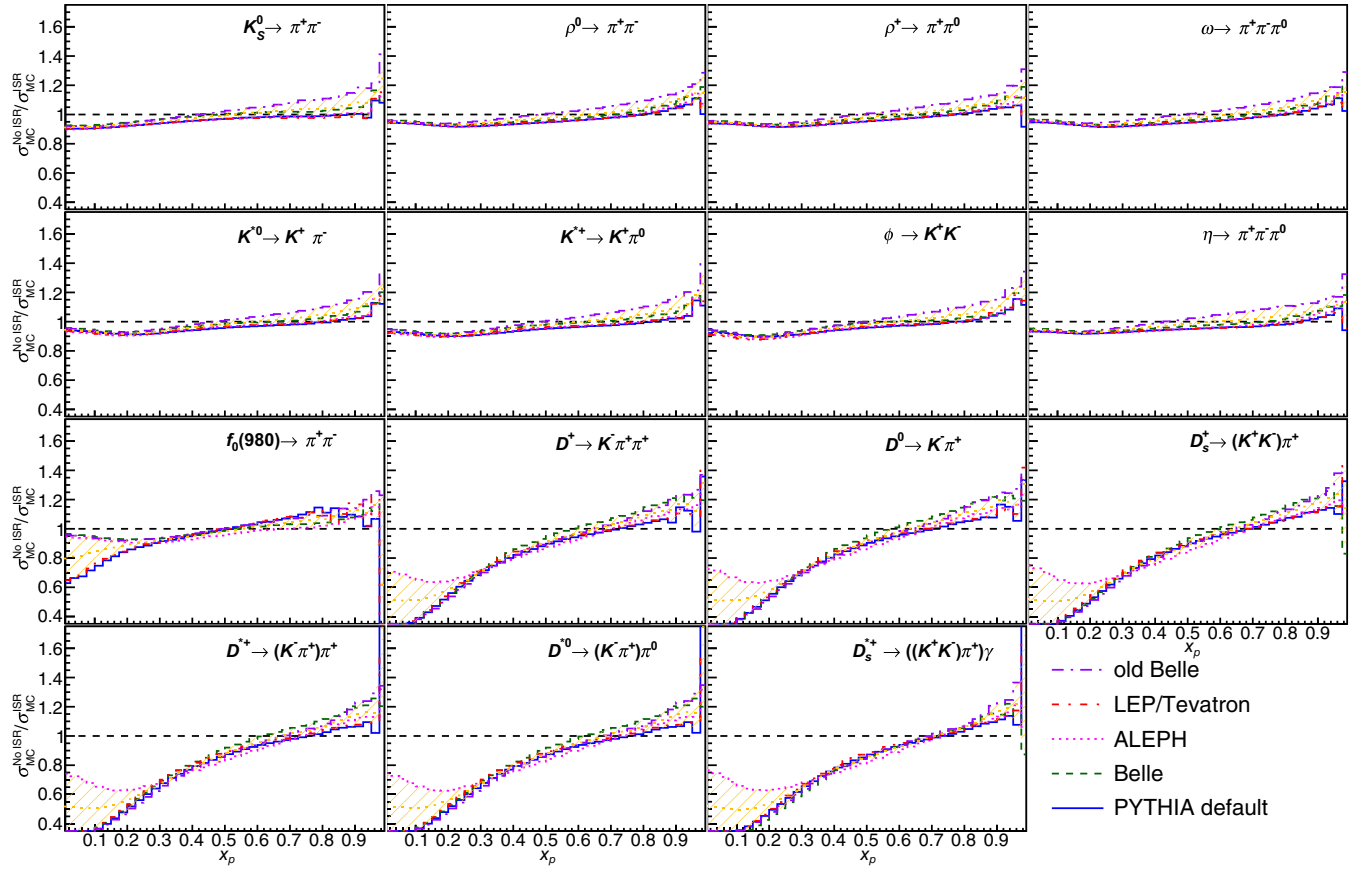
FIG. 4. ISR correction ratios as a function of x_p as evaluated by the ratio of MC-simulated yields with ISR switched off to MC simulations including ISR. To evaluate the tune dependence, various MC tunes are compared. The overall variation between them is displayed as the yellow dashed area and enters into the systematic uncertainty calculation as described in the text.

nearly 1.4 at high x_p, as can be seen in Fig. 4. Different MC tunes (cf. Table I) are investigated and show a slightly different magnitude of the ISR effects, with typically the ALEPH or old Belle tunes deviating most from the other tunes. These tune variations are again assigned as systematic uncertainties.

V. SYSTEMATIC TESTS

A. Consistency tests

The $\Upsilon(4S)$ dominantly decays into a pair of B mesons ($>96\%$ [41]). While the decay products from those can contribute at x_p of around 0.5 and below, they cannot contribute at higher x_p, given that the $\Upsilon(4S)$ and its subsequent B mesons decay nearly at rest. As such, the continuum and on-resonance data samples should be consistent for the higher x_p region. The comparison can be seen in the differential cross sections in Fig. 5 for the D mesons and in Fig. 6 for the lighter mesons. In particular for the D mesons, the different peaking structures from fragmentation at high x_p and the peaks from the $\Upsilon(4S)$ resonance and subsequent decays are clearly distinguishable. In the higher x_p region, the production cross sections are consistent with each other,

as expected. For the lighter mesons, the distinction between the two data samples is not as clearly visible as the peak in the fragmentation functions moves to much lower x_p [45]. Nevertheless, one can see the agreement at higher x_p, while at lower x_p differences due to the $\Upsilon(4S)$ decays are visible. Given the substantially larger statistical precision of the on-resonance data, which also results in reduced fluctuations in the fitted values, the final cross sections presented here use the on-resonance data for x_p above 0.55 while in the region below, the continuum data are used.

Another systematic consistency test is the comparison of the cross sections obtained from different final states for the same particle. The D^0-meson reconstruction via its $K\pi$ decay, considered here, can be compared to its reconstruction via $K\pi\pi^0$ decay as well as its two Cabibbo-suppressed $\pi\pi$ and KK decays. The cross sections for all four final states are found to be consistent with each other.

For the D_s^+ meson, the decay considered here into $\phi(\to KK)\pi$ can be compared to the $K_S^0(\to \pi\pi)K$ decay. The final state of three pions was not feasible to study due to a large background. The results from these different
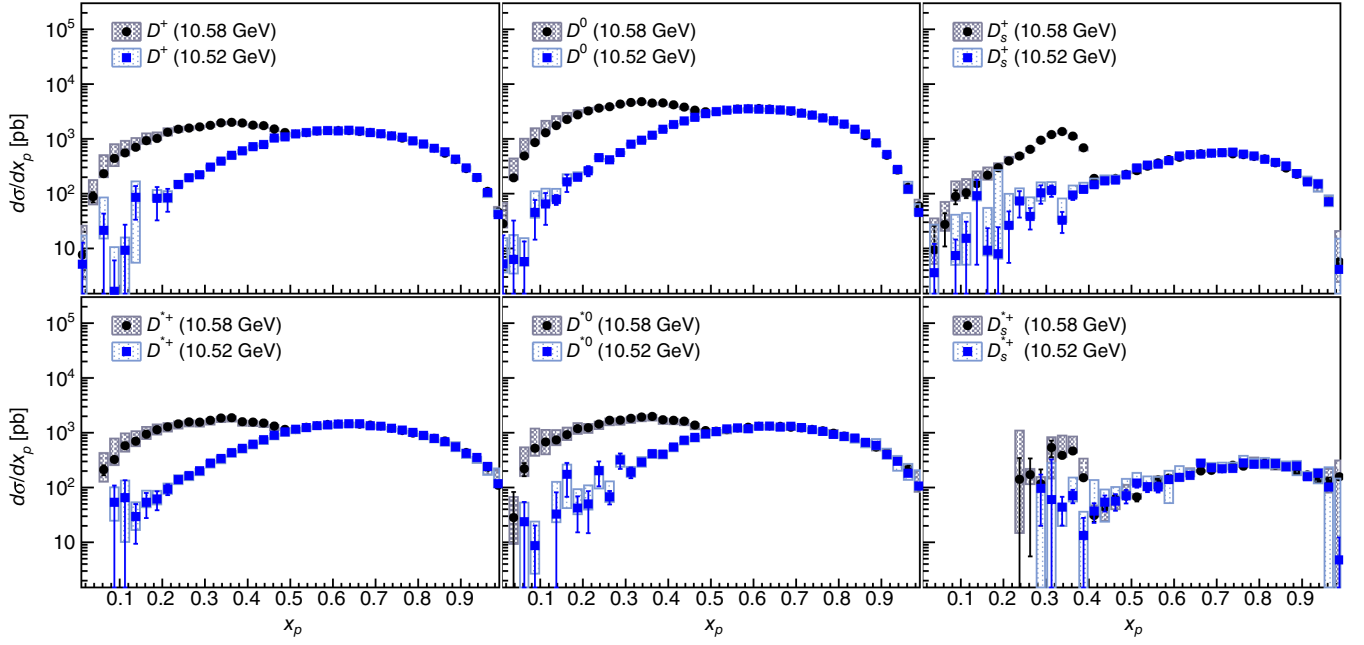
FIG. 5. Production cross sections as a function of x_p for D^+, D^0, D_s^+, D^{*+}, D^{*0}, and D_s^* for continuum (blue) and on-resonance (black) data. The low-x_p point selection is as described in the text.
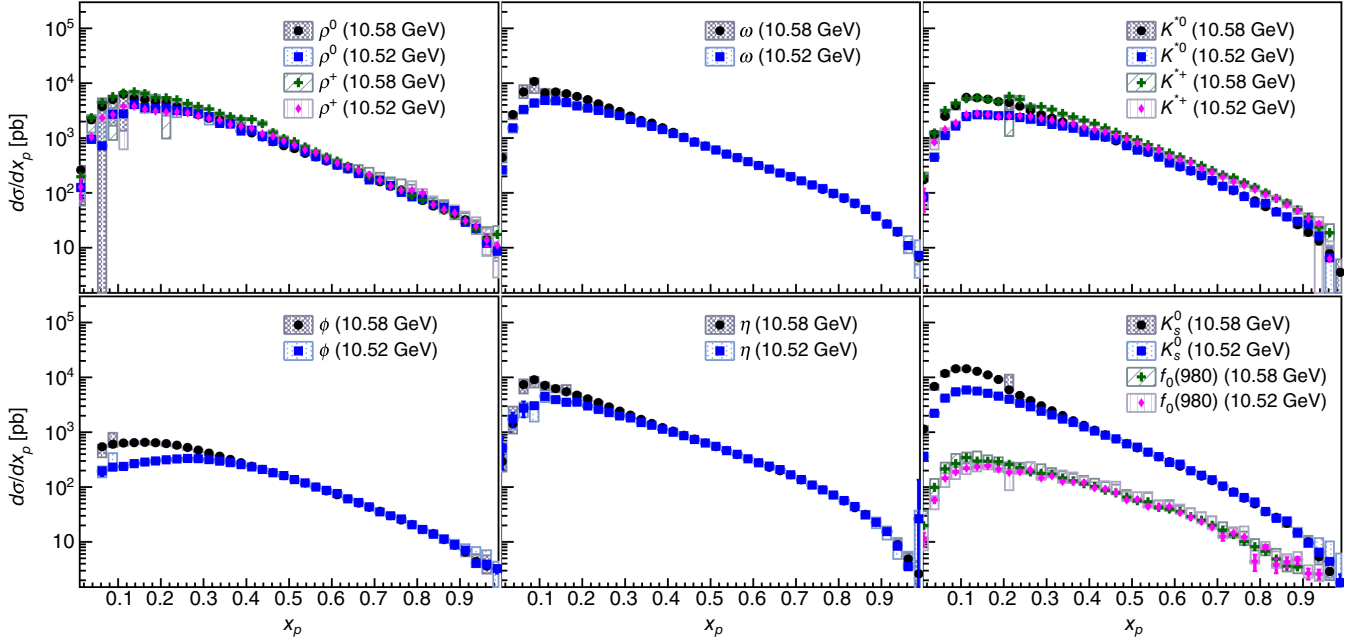

FIG. 6. Production cross sections as a function of x_p for ρ^+, ρ^0, ω, K^{*0}, K^{*+}, ϕ, η, K_S^0, and $f_0(980)$ for continuum (blue and pink points) and on-resonance (black and green points) data.

decay modes are again found to be consistent with each other within uncertainties, thus not requiring assignment of any additional systematic uncertainty.

As an additional consistency test, the neutral pions that contribute in several final states, are compared to the previously published charged-pion cross sections and found to be consistent.

B. Overall systematic uncertainties

The systematic uncertainties that are previously mentioned in the different correction steps are combined to provide the final values. They are summarized in Fig. 7 for all relevant hadrons as a function of x_p after merging the continuum and on-resonance datasets for the regions below
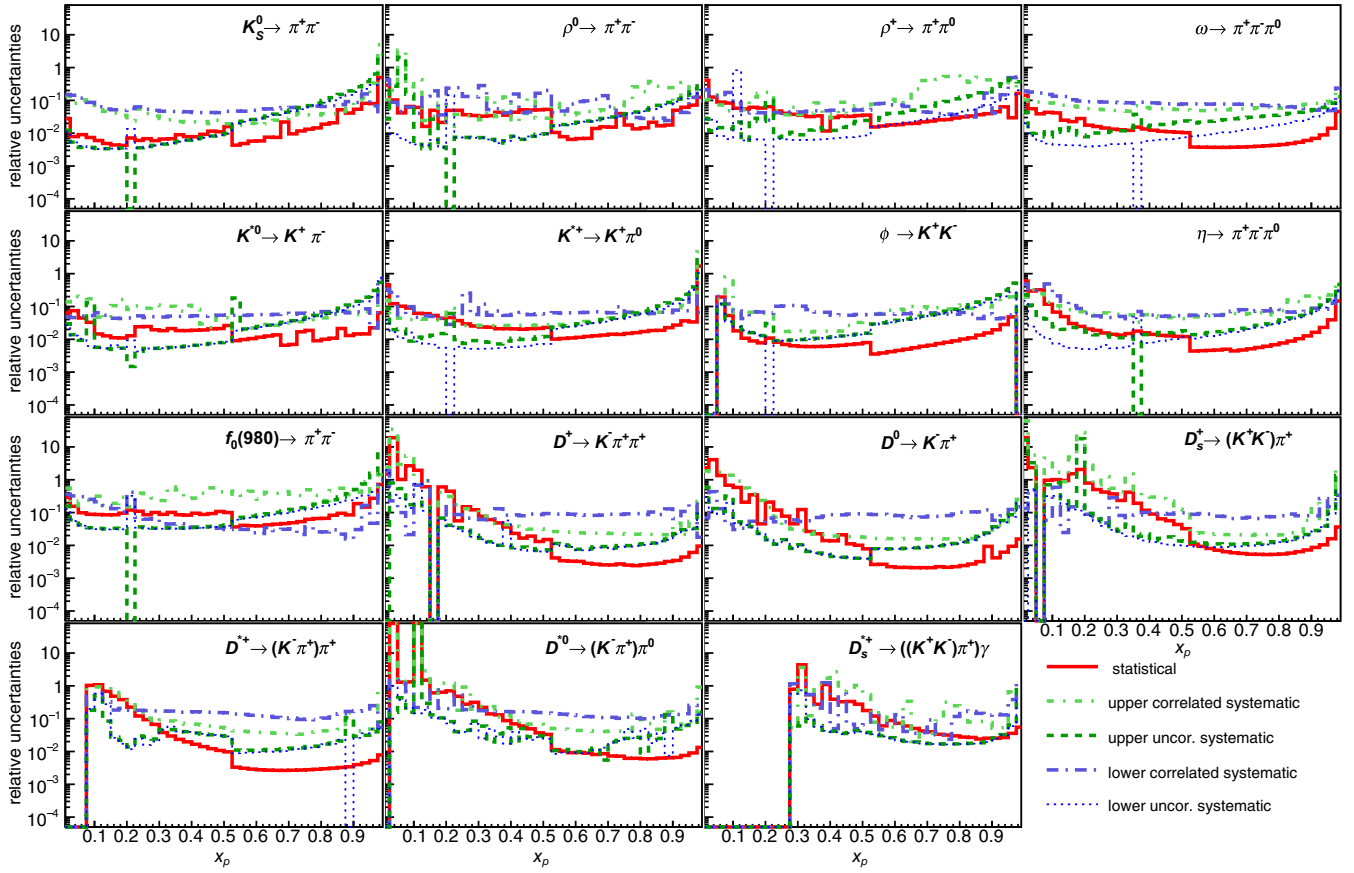
FIG. 7.   Uncertainty budgets normalized to the cross sections are shown for continuum (on-resonance) data below (above) $x_p = 0.55$ as a function of x_p. The uncertainties are displayed for statistical uncertainties (red lines), correlated upper and lower systematic uncertainties (green and blue dash-dotted lines), and uncorrelated upper and lower uncertainties (green dashed and blue dotted lines).

and above x_p of 0.55, respectively (notably visible in the drop of statistical uncertainties), and the high- and low-momentum selections where necessary. For simplicity, only the quadratic sum of all upper and lower correlated and likewise uncorrelated uncertainties are shown relative to the actual cross sections. All systematic-uncertainty contributions are separately tabulated in the Supplement Material [46], together with the cross sections. As can be seen, the measurements for all hadrons are systematics dominated. Among the systematic uncertainties, the correlated uncertainties generally dominate over the uncorrelated ones. The tune-dependent uncertainties are generally the largest, and particle-identification corrections are significant at low x_p. For D^*, and at lower x_p for lighter hadrons, the uncertainties due to the additional low-momentum efficiency corrections also contribute significantly.

A total scale uncertainty of 1.4% for the luminosity normalization and an uncertainty of 0.35% per charged decay particle from track reconstruction efficiencies is assigned. An uncertainty of 1.7% is assigned for the neutral pion reconstruction. For momenta below 200 MeV the uncertainties of 1.4% and 2.4% for charged particles and neutral pions, respectively, are assigned according to their

relative contributions in signal MC. All these uncertainties are reflected in the total systematic uncertainty budget, as shown in Fig. 7. Overall scale uncertainties arising from the limited knowledge of the branching fractions involved (cf. Table II) are kept separate to facilitate updating the results with newer branching fractions when available.

VI. RESULTS

The final results are obtained after applying all the correction steps to the fitted yields after subtracting non-$q\bar{q}$ backgrounds, namely the normalization with accumulated luminosities $\mathcal{L}$ and branching fractions $\mathcal{B}$, x_p bin widths, corrections for the acceptance and reconstruction efficiencies (ϵ_{acc}, ϵ_{rec}), additional low-momentum efficiency corrections (ϵ_{Lowp}), and the corrections for the initial-state radiation (ϵ_{ISR}) as described in the previous sections,

$$\frac{d\sigma}{dx_p} = \frac{N_{\text{Fit}} - N_{\text{non}q\bar{q}}}{\mathcal{L} \times \mathcal{B} \times \Delta x_p} \frac{1}{\epsilon_{\text{rec}} \times \epsilon_{\text{acc}} \times \epsilon_{\text{Lowp}} \times \epsilon_{\text{ISR}}}. \quad (4)$$

For the acceptance and ISR corrections, the Belle tune was chosen as the central value, while the cross sections
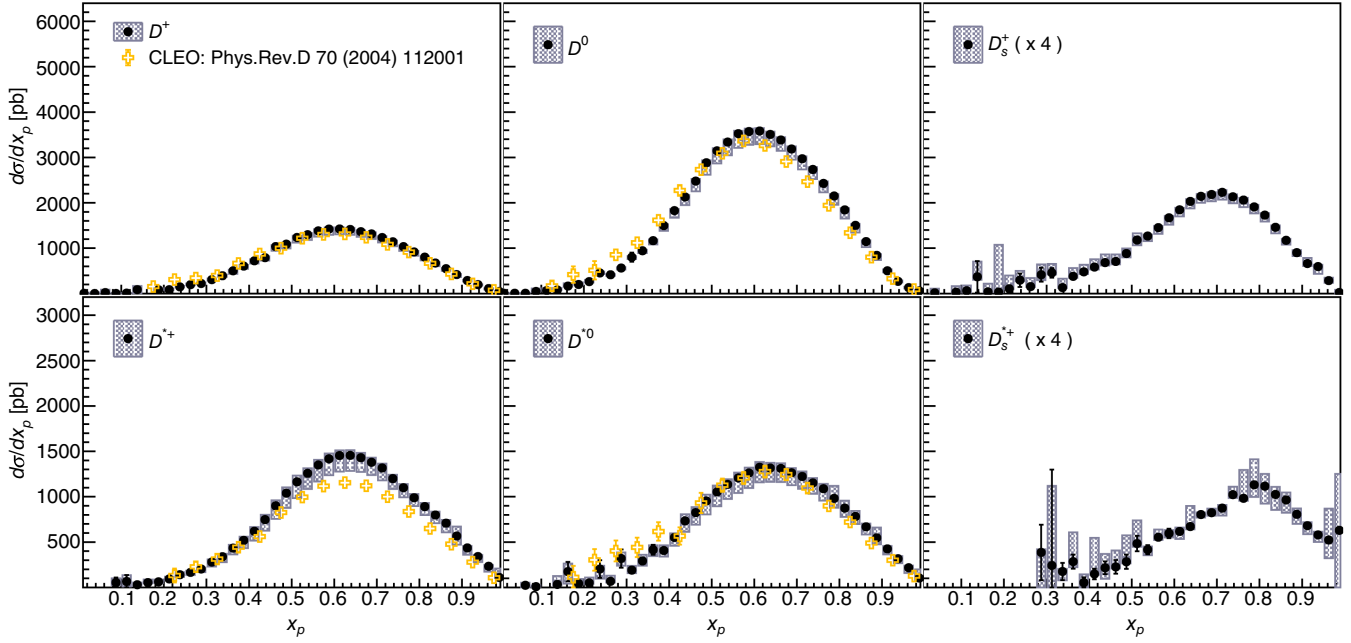
FIG. 8.   Production cross sections as a function of x_p for D^+, D^0, D_s^+, D^{*+}, D^{*0}, and D_s^*. The D_s results are scaled by a factor four for better visibility. For comparison, also the previously published results by CLEO [13] are displayed as yellow crosses, where available. The low-x_p point selection is as described in the text.

obtained from using the other tunes are tabulated in the Supplemental Material [46] and are part of the systematic uncertainties.

As apparent from Fig. 8, the charm-meson results are in good agreement with the older results from CLEO [13], particularly at larger values of x_p, with the exception of the D^{*+} which are slightly larger. They are also consistent with the previous Belle results [12] (not shown), which they supersede. In both cases, the shapes show a smaller tail than the older results at low x_p and a slightly larger tail at high x_p. These differences originate from the ISR correction, which was taken to be flat in the older publications, but found to have a distinct shape here. Before that correction, also the shapes of the old and new Belle cross sections agree quite well with each other. *BABAR* has published results on D_s meson production [14]. The integrated values for the production cross sections are consistent with the ones from Belle (taking into account the changes in the BR involved reported by the PDG between then and now). However, a comparison of the differential cross sections is hampered by unclear figure legends and an apparent lack of tabulated values.

For the light vector mesons, no previous measurements at this energy exist. Together with selected other light mesons, their production cross sections are shown in Fig. 9 as a function of the fractional momentum. As expected from local hadron parton duality [47,48], the peak of each distribution increases with the mass of the particle. For the lightest particles, the peak is at x_p around 0.1 and increases

up to 0.2 to 0.3 for heavier noncharmed particles. For D mesons it is substantially higher.

A. Isospin symmetry comparisons

Isospin symmetry should mostly hold for the FFs of the three charge-states of the ρ meson. When comparing the neutral and both charged ρ mesons, this can be confirmed for higher x_p; however at intermediate x_p an excess of up to 20% for the charged mesons is observed. In simulations, a small excess is seen due to the decays from charm production, but only at the level of a few percent maximally. A comparison of both charged and neutral ρ mesons is displayed in Fig. 10.

For K^*, the fragmentation functions should also be isospin symmetric. However, in the initial process during e^+e^- annihilation, due to the charge factor, $u\bar{u}$ and $d\bar{d}$ pairs are not produced equally, resulting in a difference in the cross sections. This is not the case for pions or ρ mesons as the initially produced quark-antiquark pair always provides a matching valence-parton. In the MC, the fragmentation from strange quarks appears to be equal for both the neutral and charged kaons, but the differences in initial up and down quarks result in an enhancement of charged K^* production that is increasing with x_p. This increase at higher x_p is expected as the favored fragmentation (where the fragmenting quark is a valence particle in the detected hadron) from the initial up or down quark is larger there, as discussed for example in Ref. [49]. This is also observed in the data where the cross sections are comparable at
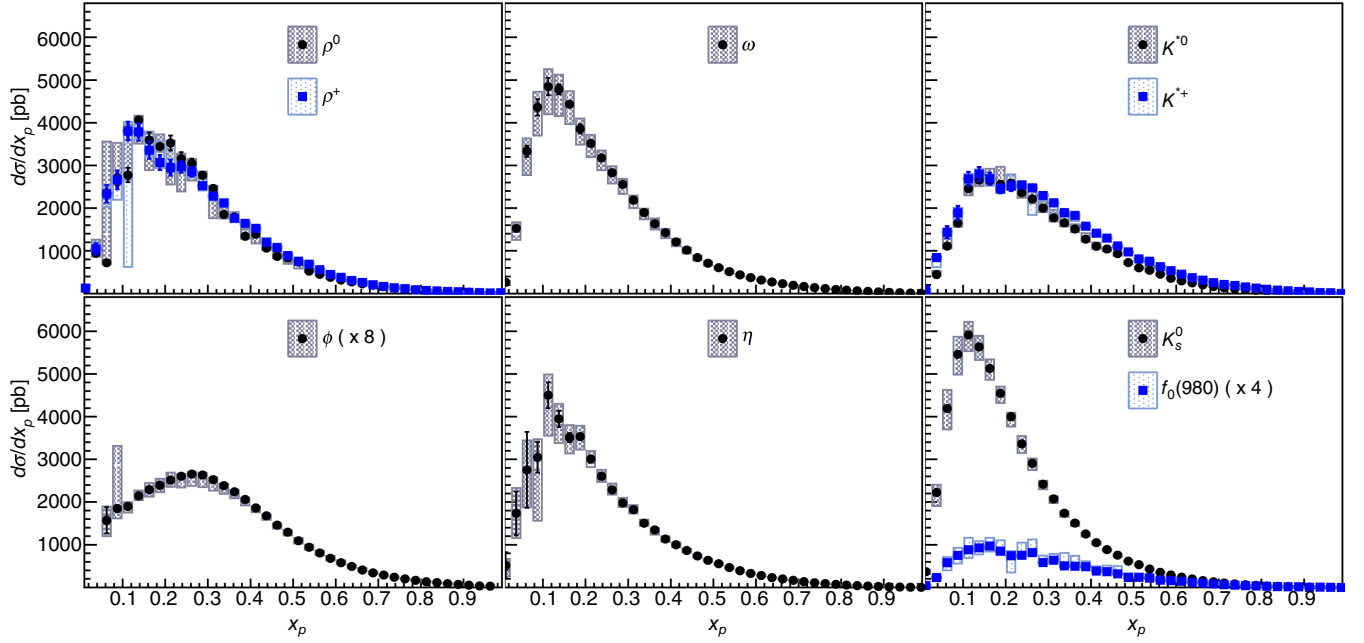
FIG. 9. Production cross sections as a function of x_p for ρ^+, ρ^0, ω, K^{*+}, K^{*0}, ϕ, η, K_S^0, and $f_0(980)$. The ϕ and $f_0(980)$ cross sections are scaled by a factor of 8 and 4, respectively, for better visibility.
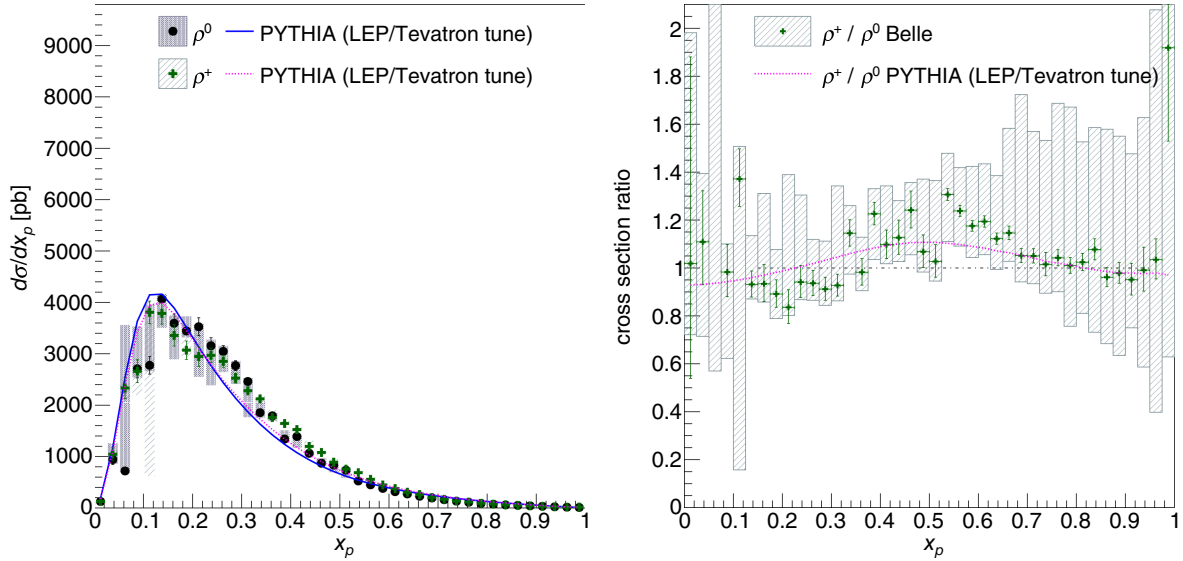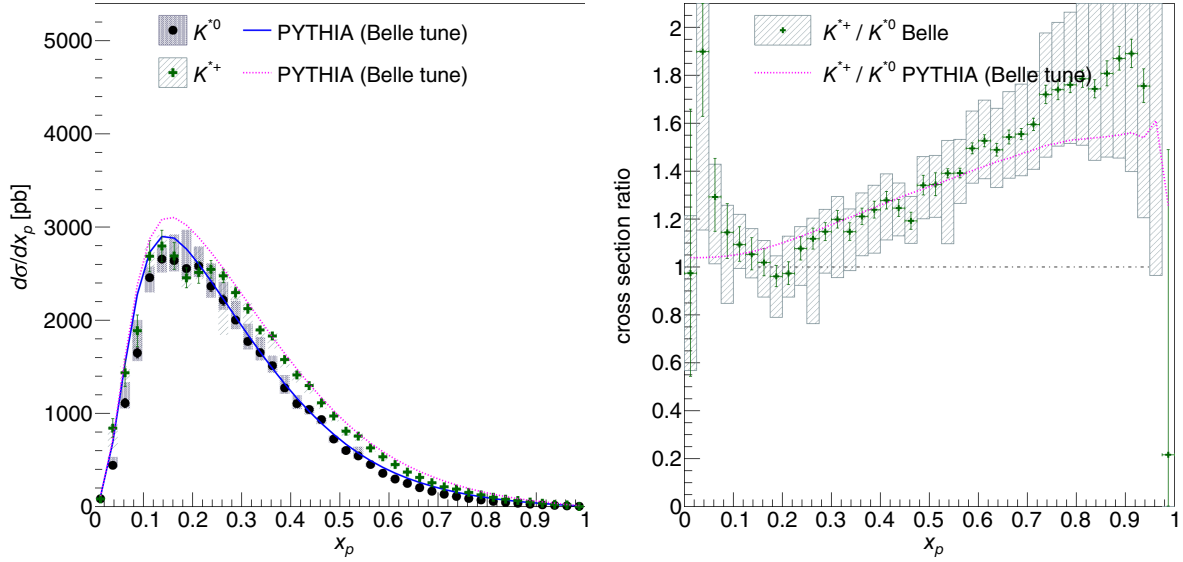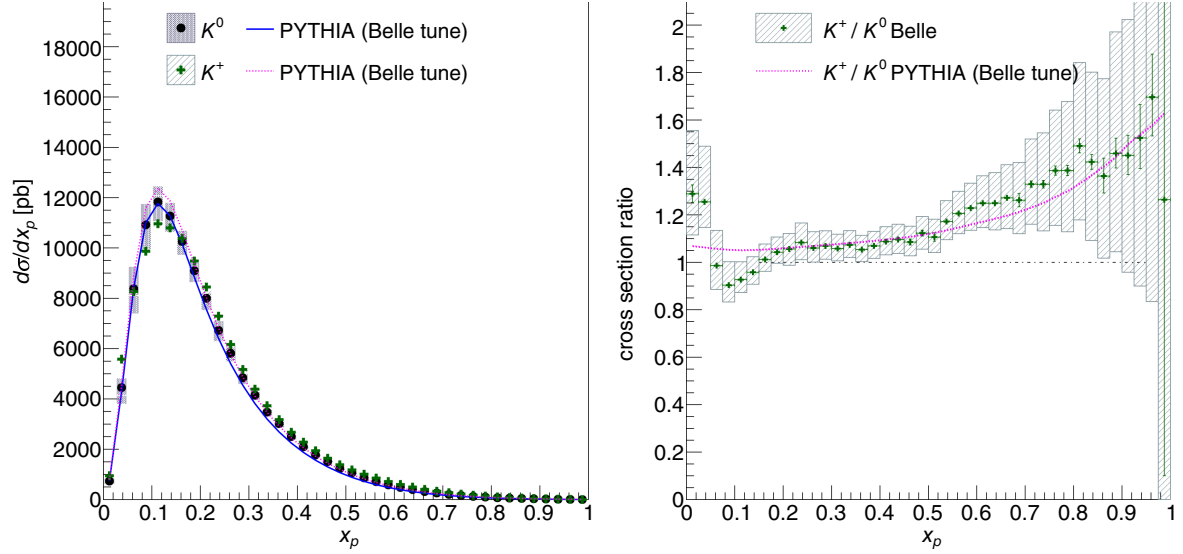

FIG. 10. Left: comparison of neutral and charged ρ meson cross sections for both the Belle data and a PYTHIA MC simulation using the LEP/Tevatron fragmentation tune. Right: corresponding ratios of charged to neutral ρ cross sections, both for Belle data and MC.

low x_p but an excess of charged K^* is visible and increasing with x_p, as expected. These comparisons are displayed in Fig. 11.

A similar, but slightly less pronounced behavior is also seen for the pseudoscalar kaons, where the differences amount to about 5% at intermediate x_p and are also consistent with MC expectations. Those are shown in Fig. 12.

B. Direct vector vs pseudoscalar fragmentation studies

For the lighter mesons, it is of interest to compare the differential cross sections of *promptly* produced light pseudoscalar and vector mesons. Cross sections for ρ, ω, K^*, and ϕ are shown in Fig. 13 in comparison to η, K^0 as well as charged pions and kaons. The charged pions and kaons are extracted here in an x_p binning while the previously published cross sections [29] were binned in

FIG. 11.   Left: comparison of neutral and charged K^* meson cross sections for both the Belle data and a PYTHIA MC simulation using the Belle fragmentation tune. Right: corresponding ratios of charged to neutral K^* cross sections, both for Belle data and MC.

FIG. 12.   Left: comparison of neutral and charged K meson cross sections for both the Belle data and a PYTHIA MC simulation using the Belle fragmentation tune. Right: corresponding ratios of charged to neutral K cross sections, both for Belle data and MC.

the energy fraction. For these *direct* production rates, the feed-down contributions from all the final states considered in this analysis are subtracted, based on their measured cross sections and MC-based x_p migration matrices between parent and daughter particles. It should be noted that such feed-down subtracted cross sections do not fulfill the formal definitions of fragmentation functions, which are inclusive objects including all strong decays. They nevertheless indicate the differences in direct fragmentation, which may be relevant to fragmentation settings in MC event generators.

To compare similar quantities, the average of positive and negative pions is taken to compare to the ρ^+ and ρ^0 mesons. It can be seen that at high x_p, pions and the ρ vector mesons have more similar cross sections, suggesting that light pseudoscalar and vector mesons are produced about equally in fragmentation. At lower x_p, the decays from other particles, which are not accounted for here, contribute to pions and thus their cross sections start exceeding those of the vector mesons significantly. Based on MC studies, the fraction of unaccounted for contributions is below 60% of the actual directly produced
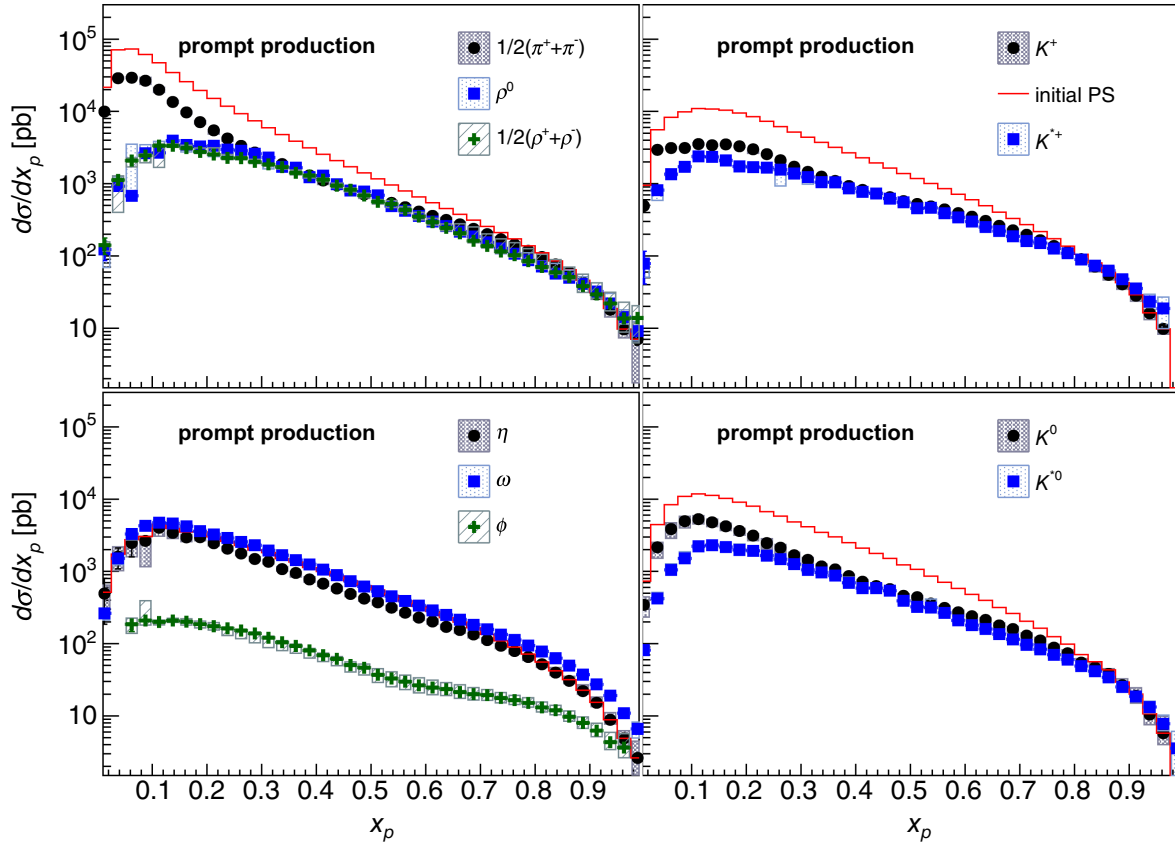
FIG. 13. Comparison of x_p differential prompt production rates for pseudoscalar mesons to those for vector-meson cross sections after subtracting the contributions from decays of the parent-particles analyzed in this work into these final particles. The red histograms indicate the cross sections of the corresponding pseudoscalar mesons before subtraction. Top left: comparison of charge-averaged charged pions (black points) to charge-averaged charged ρ mesons (dark green, upward triangles), and ρ^0 (blue squares). Top right: comparison of charged kaons (black points) to K^{*+} (blue squares). Bottom left: ω (black points), η (blue squares), and ϕ (dark green, upward triangles). Bottom right: K^0 (black points) and K^{*0} (blue squares).

yields for pions, while it is much lower for ρ mesons. However, even in the MC the missing feed-down does not appear to be the main cause of the differences, suggesting that the fairly large mass difference between pions and ρ mesons is more relevant at low x_p for fragmentation.

For kaons, the comparison between pseudoscalar and vector mesons shows a similar behavior. The charged mesons are again on a similar level at intermediate x_p. The pseudoscalar meson cross sections start exceeding the vector mesons again at lower x_p due to the additional decays, but to a lesser extent than for pions. The MC-based fractions of unaccounted for contributions are smaller here, reaching up to 25% for pseudoscalar kaons and even less for other particles. For a consistent comparison of the neutral kaons, all K^0 are displayed, based on scaling the K^0_S measurements by a factor of 2 to include the unaccounted K^0_L contribution. The η mesons appear to be generally suppressed compared to ω mesons, but their shapes are similar. As the contribution from η' decay is not subtracted here, the direct fragmentation into η is even lower (possibly by a factor of more than two, according to

MC simulations). The ϕ mesons are further suppressed, as expected due to the additional strangeness that needs to be created in the fragmentation process.

Similar comparisons between pseudoscalar and vector mesons are presented in Fig. 14 for the charmed mesons. Also in this case, the feed-down from the higher-mass vector mesons analyzed here have been subtracted, with nearly all D^* mesons decaying into pseudoscalar D mesons. An increased fragmentation for charmed vector compared to pseudoscalar mesons is clearly visible. This is consistent with what most MC generators generally have as their default settings for charm fragmentation. In the case of D^+_s, while the overall size is similar to that of the D^{*+}_s, a pronounced difference in the x_p shape is visible with the D^{*+}_s peaking at substantially larger x_p than the D^+_s cross section.

Additionally, isospin symmetry appears to be roughly fulfilled for both D^* as well as pseudoscalar D mesons, despite the initial cross sections before feed-down correction being significantly larger for neutral D mesons. The latter appear slightly larger but are within the uncertainties
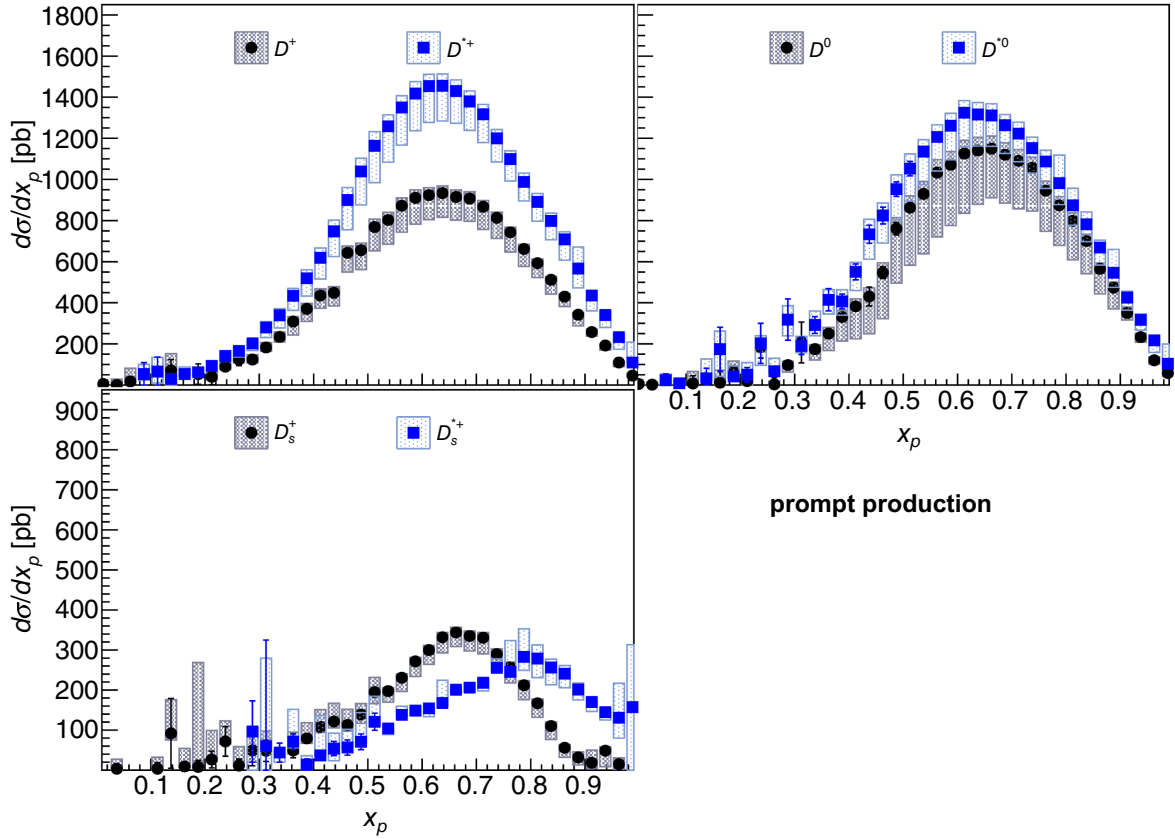
FIG. 14.   Comparison of pseudoscalar meson cross sections to vector-meson cross sections for various charmed mesons after subtracting the contributions from all decays of the parent-particles analyzed in this study.

that mostly originate from the parent D^* uncertainties. A similar observation was already made in a previous publication [12].

C. Tune comparisons

As discussed in the previous sections about acceptance and ISR corrections, various PYTHIA tunes are used to estimate the dependence of these corrections on the description of the fragmentation itself. It follows that these tunes can also be compared to the final results to learn which parameters in PYTHIA6 do best in describing fragmentation. For the D meson results, the most relevant parameters are the Lund-model parameters related to the mass (PARJ 42), the high-x_p behavior (PARJ 41), and the transverse momentum produced in the fragmentation (PARJ 21). In Fig. 15, all tunes display the typical peaking behavior of the inclusive cross sections, but the peak positions vary significantly. The HERMES tune has the highest suppression at high x_p (PARJ 41 of 1.94) and therefore peaks at the lowest values, far away from the actual data. All other tunes are not only closer together (with PARJ 41 values ranging from 0.3 to 0.5), but are generally closer to the data. Apart from the absolute magnitude, the default PYTHIA and Belle-related tunes reproduce the shape and

peak position best, while LEP and ALEPH tunes either peak at lower x_p or higher x_p, respectively. One striking exception is the behavior of the strange D mesons, where only the ALEPH tune is able to roughly reproduce the peak position. Furthermore, apart from the LEP tune, all tunes largely overestimate the overall magnitude. This suggests that the additional strangeness further pushes the peak to higher x_p and suppresses the production cross section [50]. Figure 16 displays the different tunes for the charmed mesons relative to the measured cross sections.

Part of the magnitude differences between the tunes and the data for all D mesons can be related to the probability of producing a charmed vector meson over a pseudoscalar meson, which is encoded in PARJ 13. From these magnitude comparisons, it appears that tunes for which this parameter ranges from PARJ 13 of 0.65 to 0.75 are preferred over the LEP tune (0.54). This is roughly consistent with the optimization efforts reported in [12] where a best value of 0.59 was found.

Turning to the lighter mesons, more parameters are needed in the description of the fragmentation process. In the case of the vector mesons, the aforementioned ratio between vector meson and pseudoscalar meson production is again very relevant. For light quarks, this is encoded in PARJ 11 and for strange quarks in PARJ 12. The default
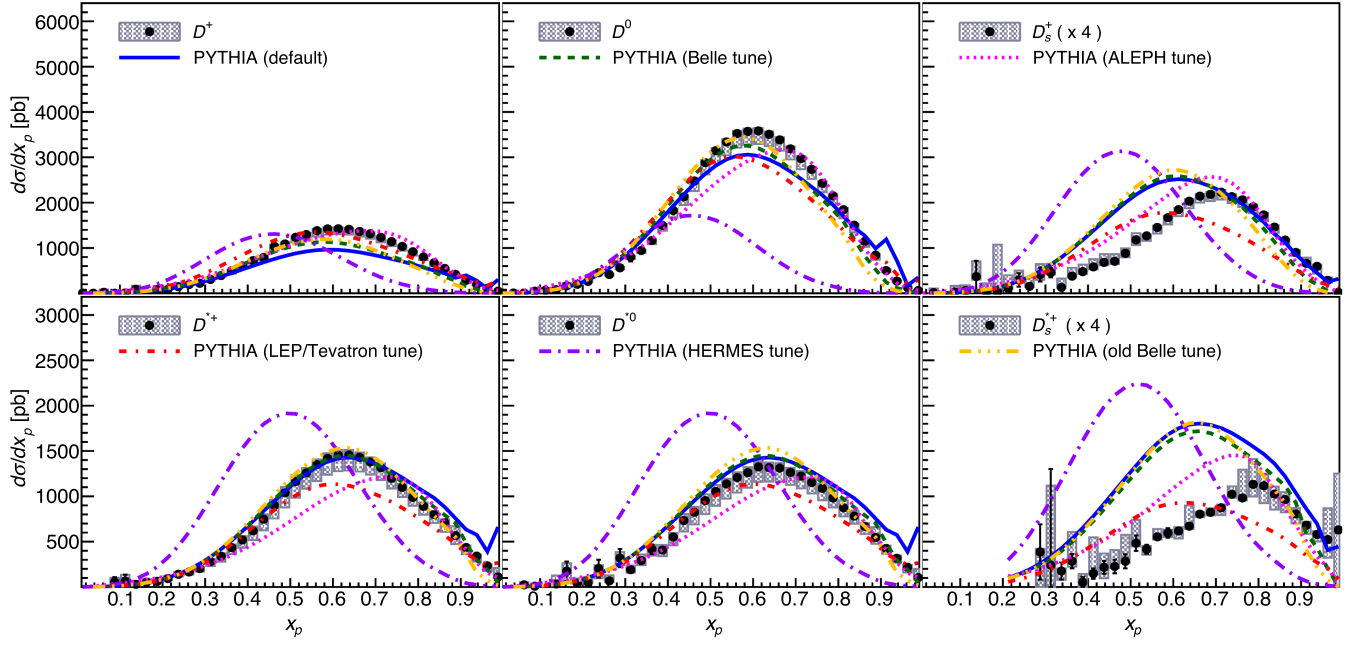
FIG. 15. Production cross sections as a function of x_p for D^+, D^0, D_s^+, D^{*+}, D^{*0}, and D_s^{*+} shown for data (black points), compared to various PYTHIA tunes as described in the text. The D_s cross sections are scaled by a factor of 4. The low-x_p point selection is as described in the text.
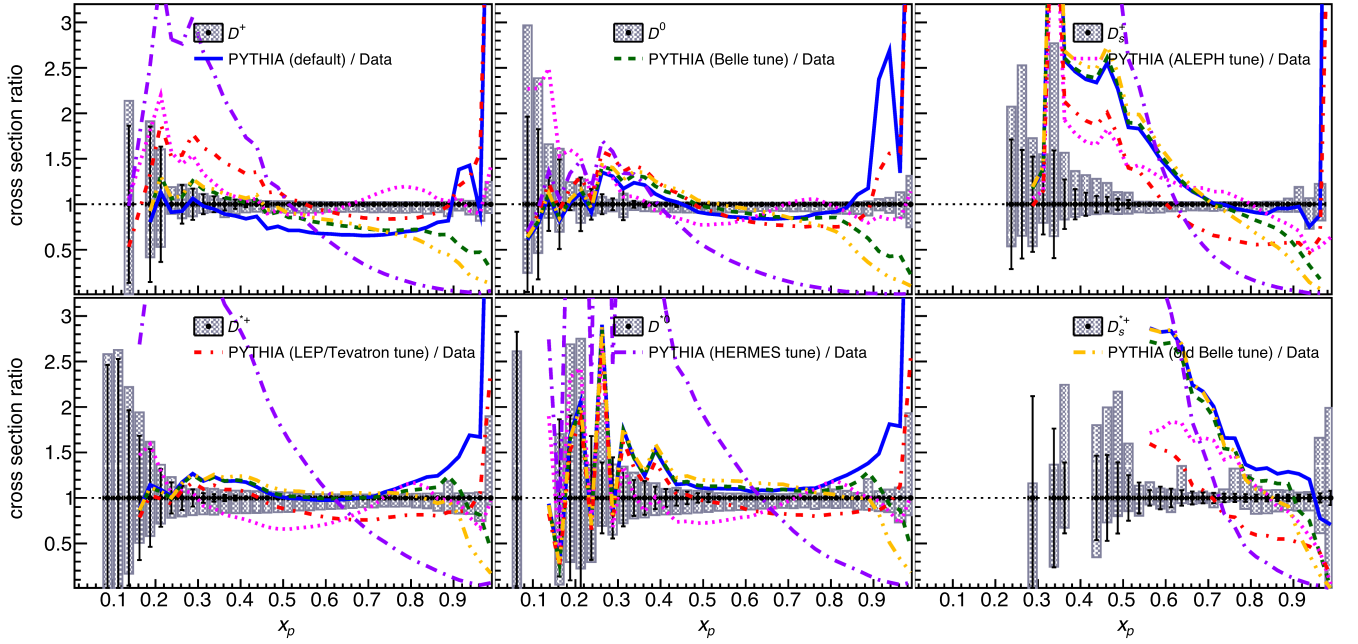

FIG. 16. Production cross sections for D^+, D^0, D_s^+, D^{*+}, D^{*0}, and D_s^{*+} from MC simulations using various fragmentation tunes (as indicated) relative to Belle data as a function of x_p. The data points and uncertainty boxes display the relative uncertainties of the data, whose values are suppressed for clarity when exceeding the scale of the plot.

values are 0.5 for light quarks and 0.6 for strange quarks. To study the effect of an increase in the ratio, the default PYTHIA setting was also tested with the light-quark ratio set to 0.6, labeled *high VM* in Fig. 17. Figure 18 also displays the different tunes for the noncharmed mesons relative to

the measured inclusive data. The cross sections for ρ and ω mesons are indeed predicted to be slightly larger than in the default setting. However, from the measured data there does not appear to be a need to increase this fraction, which is consistent with the feed-down subtracted comparisons
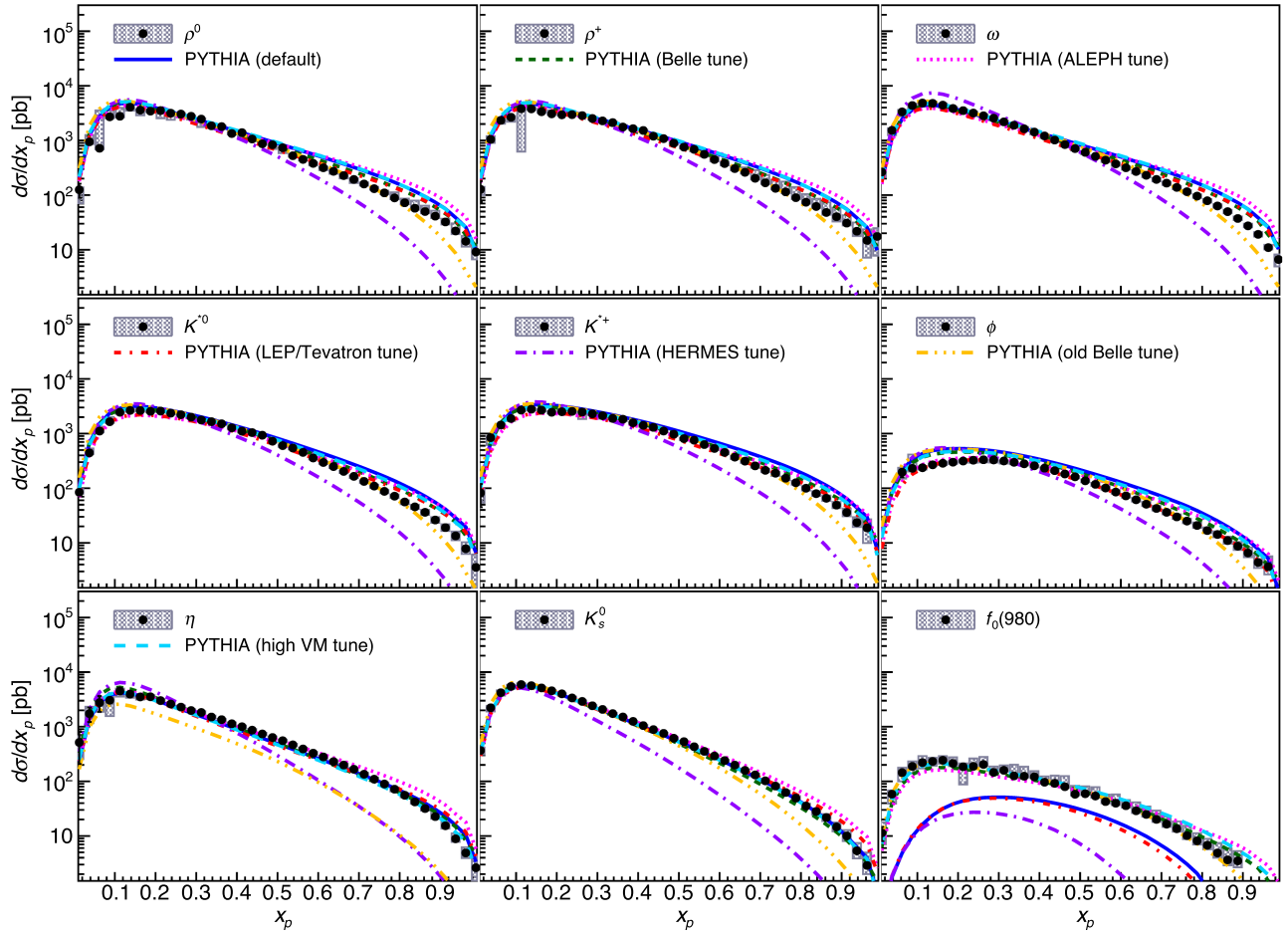
FIG. 17.   Production cross sections as a function of x_p for ρ^0, ρ^+, ω, K^{*0}, K^{*+}, ϕ, η, K_S^0, and $f_0(980)$ for data (black points) compared to various MC tunes as discussed in the text.
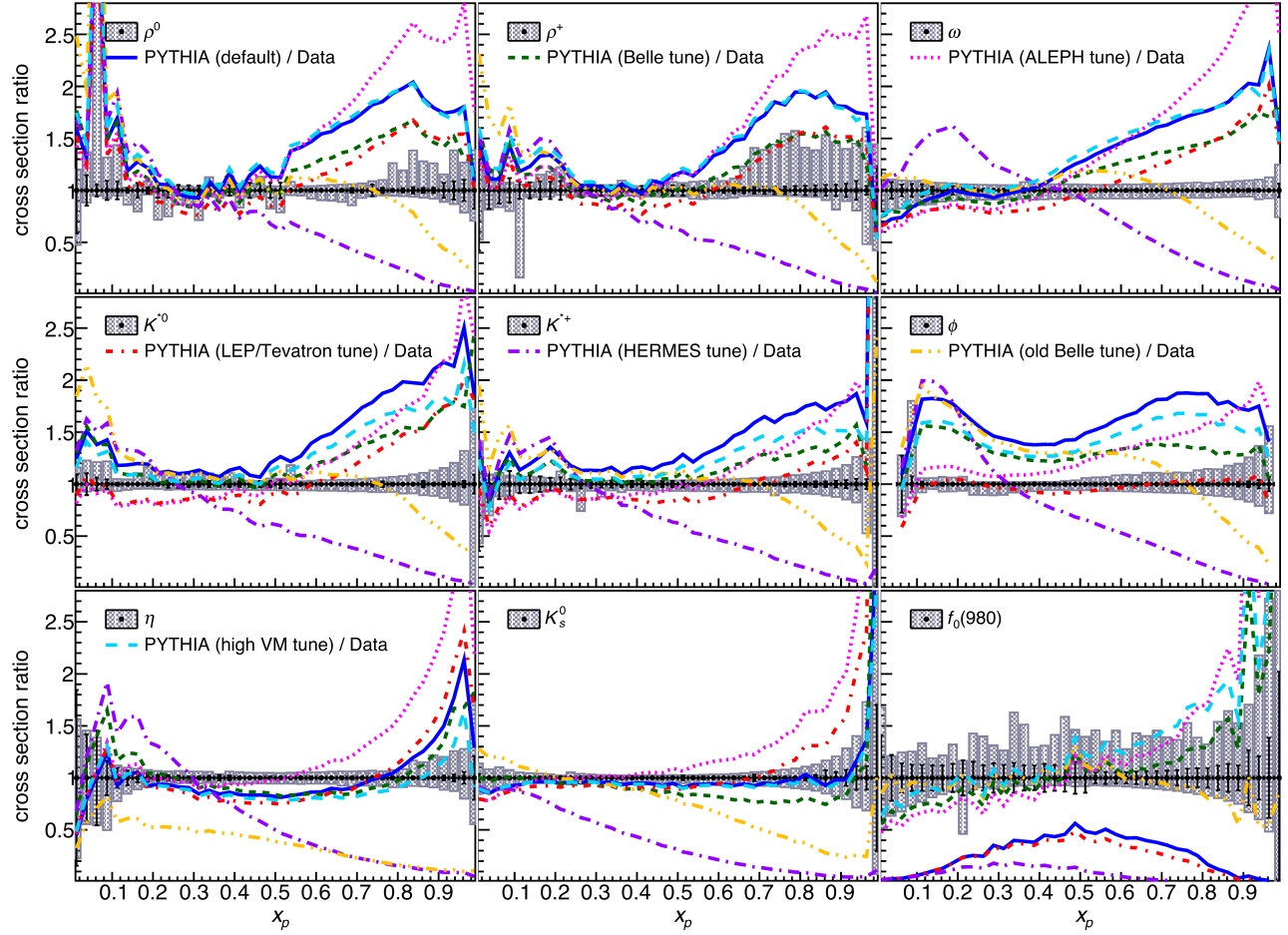
FIG. 18. Production cross sections for ρ^0, ρ^+, ω, K^{*0}, K^{*+}, ϕ, η, K_S^0, and $f_0(980)$ from MC simulations using various fragmentation tunes (as indicated) relative to Belle data as a function of x_p.

discussed above. Overall, the magnitudes, and partially the shapes, of the cross sections are described reasonably well, with the ALEPH, default PYTHIA, and LEP tunes producing slightly harder, and the old Belle and (in particular) HERMES tunes producing softer distributions.

VII. SUMMARY

In summary, we have reported the differential production cross sections in e^+e^- annihilation near $\sqrt{s} = 10.58$ GeV as a function of the momentum fraction x_p for ρ^+, ρ^0, ω, K^{*+}, K^{*0}, ϕ, η, K_S^0, $f_0(980)$, D^+, D^0, D_s^+, D^{*+}, D^{*0}, and D_s^{*+}. The charmed-meson results provide an update of the previous Belle measurement, which they supersede, while the D_s^{*+} meson cross sections are measured for the first time in Belle. Cross sections for vector mesons as well as those for η, and K_S^0 are obtained for the first time at B factories and provide additional insight into the modeling of fragmentation, particularly concerning the role of the spin of the final-state particle and its mass and fractional-momentum dependence. From these results it is concluded that no additional enhancement of spin-one fragmentation

over spin-zero particles is needed in the PYTHIA MC event generators. These results will also serve as valuable input for the modeling of ultra-high-energetic cosmic air showers as it relates to the impact of fragmentation on the number of detected muons at the Earth's surface.

The results will impact the use of the mesons studied here in, e.g., the investigation of spin-dependent fragmentation in semi-inclusive deep inelastic scattering, where new insights can also be gained about the spin structure of the nucleon.

DATA AVAILABILITY

The data that support the findings of this article are openly available [46].

[1] J. Collins, Foundations of perturbative QCD, Cambridge Monogr. Part. Phys., Nucl. Phys., Cosmol. **32**, 1 (2011).

[2] A. Accardi *et al.*, Electron ion collider: The next QCD frontier: Understanding the glue that binds us all, Eur. Phys. J. A **52**, 268 (2016).

[3] R. Abdul Khalek *et al.*, Science requirements and detector concepts for the electron-ion collider: EIC yellow report, Nucl. Phys. **A1026**, 122447 (2022).

[4] R. Brandelik *et al.* (TASSO Collaboration), Charged pion, kaon, proton and anti-proton production in high-energy e^+e^- annihilation, Phys. Lett. **94B**, 444 (1980).

[5] M. Althoff *et al.* (TASSO Collaboration), Charged hadron composition of the final state in e^+e^- annihilation at high energies, Z. Phys. C **17**, 5 (1983).

[6] H. Aihara *et al.* (TPC/Two Gamma Collaboration), Charged hadron inclusive cross-sections and fractions in e^+e^- annihiliation $\sqrt{s} = 29$ GeV, Phys. Rev. Lett. **61**, 1263 (1988).

[7] D. Buskulic *et al.* (ALEPH Collaboration), Inclusive $\pi^{\pm}$, $K^{\pm}$ and $(p, \bar{p})$ differential cross-sections at the Z resonance, Z. Phys. C **66**, 355 (1995).

[8] P. Abreu *et al.* (DELPHI Collaboration), $\pi^{\pm}$, $K^{\pm}$, p and $\bar{p}$ production in $Z^0 \to q\bar{q}$, $Z^0 \to b\bar{b}$, $Z^0 \to u\bar{u}, d\bar{d}, s\bar{s}$, Eur. Phys. J. C **5**, 585 (1998).

[9] K. Abe *et al.* (SLD Collaboration), Production of π^+, π^-, K^+, K^-, p and $\bar{p}$ in light (uds), c and b jets from Z^0 decays, Phys. Rev. D **69**, 072003 (2004).

[10] J. P. Lees *et al.* (*BABAR* Collaboration), Production of charged pions, kaons, and protons in e^+e^- annihilations into hadrons at $\sqrt{s} = 10.54$ GeV, Phys. Rev. D **88**, 032011 (2013).

[11] M. Leitgab *et al.* (Belle Collaboration), Precision measurement of charged pion and kaon differential cross sections in e^+e^- annihilation at $\sqrt{s} = 10.52$ GeV, Phys. Rev. Lett. **111**, 062002 (2013).

[12] R. Seuster *et al.* (Belle Collaboration), Charm hadrons from fragmentation and B decays in e^+e^- annihilation at $\sqrt{s} = 10.6$ GeV, Phys. Rev. D **73**, 032002 (2006).

[13] M. Artuso *et al.* (CLEO Collaboration), Charm meson spectra in e^+e^- annihilation at 10.5-GeV c.m.e., Phys. Rev. D **70**, 112001 (2004).

[14] B. Aubert *et al.* (*BABAR* Collaboration), Measurement of D_s^+ and D_s^{*+} production in *B* meson decays and from continuum e^+e^- annihilation at $\sqrt{s} = 10.6$ GeV, Phys. Rev. D **65,** 091104 (2002).

[15] M. Ablikim *et al.* (BESIII Collaboration), Measurements of normalized differential cross sections of inclusive π^0 and K_S^0 production in e^+e^- annihilation at energies from 2.2324 to 3.6710 GeV, Phys. Rev. Lett. **130,** 231901 (2023).

[16] M. Ablikim *et al.* (BESIII Collaboration), Measurements of normalized differential cross sections of inclusive η production in e^+e^- annihilation at energy from 2.0000 to 3.6710 GeV, Phys. Rev. Lett. **133,** 021901 (2024).

[17] P. Abreu *et al.* (DELPHI Collaboration), Measurement of inclusive ρ^0, $f_0(980)$, $f_2(1270)$, $K_2^{*0}(1430)$ and $f_2'(1525)$ production in Z^0 decays, Phys. Lett. B **449,** 364 (1999).

[18] K. Ackerstaff *et al.* (OPAL Collaboration), Production of $f_0(980)$, $f_2(1270)$ and $\phi(1020)$ in hadronic Z^0 decay, Eur. Phys. J. C **4,** 19 (1998).

[19] T. Sjöstrand, L. Lönnblad, and S. Mrenna, PYTHIA6.2: Physics and manual, arXiv:hep-ph/0108264.

[20] T. Sjöstrand, P. Eden, C. Friberg, L. Lönnblad, G. Miu, S. Mrenna, and E. Norrbin, High-energy physics event generation with PYTHIA 6.1, Comput. Phys. Commun. **135,** 238 (2001).

[21] J. Albrecht *et al.*, The muon puzzle in cosmic-ray induced air showers and its connection to the Large Hadron Collider, Astrophys. Space Sci. **367,** 27 (2022).

[22] S. Ostapchenko, QGSJET-II: Physics, recent improvements, and results for air showers, EPJ Web Conf. **52,** 02001 (2013).

[23] F. Riehn, R. Engel, A. Fedynitch, T. K. Gaisser, and T. Stanev, Hadronic interaction model Sibyll 2.3d and extensive air showers, Phys. Rev. D **102,** 063002 (2020).

[24] J. C. Collins, Fragmentation of transversely polarized quarks probed in transverse momentum distributions, Nucl. Phys. **B396,** 161 (1993).

[25] X. Artru, String fragmentation model with quark spin, Prob. At. Sci. Technol. **2012N1,** 173 (2012).

[26] X. Artru and G. Mennessier, String model and multiproduction, Nucl. Phys. **B70,** 93 (1974).

[27] A. Kerbizi, X. Artru, and A. Martin, Production of vector mesons in the String $+ ^3P_0$ model of polarized quark fragmentation, Phys. Rev. D **104,** 114038 (2021).

[28] G. D. Alexeev *et al.*, Collins and Sivers transverse-spin asymmetries in inclusive muoproduction of ρ^0 mesons, Phys. Lett. B **843,** 137950 (2023).

[29] R. Seidl *et al.* (Belle Collaboration), Update of inclusive cross sections of single and pairs of identified light charged hadrons, Phys. Rev. D **101,** 092004 (2020).

[30] A. Abashian *et al.*, The Belle detector, Nucl. Instrum. Methods Phys. Res., Sect. A **479,** 117 (2002).

[31] J. Brodzicka *et al.* (Belle Collaboration), Physics achievements from the Belle experiment, Prog. Theor. Exp. Phys. **2012,** 04D001 (2012).

[32] S. Kurokawa and E. Kikutani, Overview of the KEKB accelerators, Nucl. Instrum. Methods Phys. Res., Sect. A **499,** 1 (2003).

[33] T. Abe *et al.*, Achievements of KEKB, Prog. Theor. Exp. Phys. **2013,** 03A001 (2013).

[34] T. Sjöstrand, S. Mrenna, and P. Z. Skands, PYTHIA 6.4 physics and manual, J. High Energy Phys. 05 (2006) 026.

[35] D. J. Lange, The EvtGen particle decay simulation package, Nucl. Instrum. Methods Phys. Res., Sect. A **462,** 152 (2001).

[36] F. A. Berends, P. H. Daverveldt, and R. Kleiss, Monte Carlo simulation of two photon processes. 2. Complete lowest order calculations for four lepton production processes in electron positron collisions, Comput. Phys. Commun. **40,** 285 (1986).

[37] S. Jadach, J. H. Kühn, and Z. Wąs, TAUOLA: A library of Monte Carlo programs to simulate decays of polarized tau leptons, Comput. Phys. Commun. **64,** 275 (1990).

[38] R. Brun, F. Bruyant, F. Carminati, S. Giani, M. Maire, A. McPherson, G. Patrick, and L. Urban, Geant detector description and simulation tool, 10.17181/CERN.MUHF.DMJ1 (1994).

[39] S. Brandt, C. Peyrou, R. Sosnowski, and A. Wroblewski, The principal axis of jets. An attempt to analyze high-energy collisions as two-body processes, Phys. Lett. **12,** 57 (1964).

[40] Throughout this manuscript *c* is set to unity.

[41] S. Navas *et al.* (Particle Data Group), Review of particle physics, Phys. Rev. D **110,** 030001 (2024).

[42] R. Seidl *et al.* (Belle Collaboration), Invariant-mass and fractional-energy dependence of inclusive production of dihadrons in e^+e^- annihilation at $\sqrt{s} = 10.58$ GeV, Phys. Rev. D **96,** 032005 (2017).

[43] P. Soeding, On the apparent shift of the rho meson mass in photoproduction, Phys. Lett. **19,** 702 (1966).

[44] B. I. Abelev *et al.* (STAR Collaboration), ρ^0 photoproduction in ultraperipheral relativistic heavy ion collisions at $\sqrt{s_{NN}} = 200$ GeV, Phys. Rev. C **77,** 034910 (2008).

[45] S. Albino, B. A. Kniehl, G. Kramer, and W. Ochs, The evolution of hadron spectra in the modified leading logarithm approximation, Eur. Phys. J. C **36,** 49 (2004).

[46] See Supplemental Material at http://link.aps.org/supplemental/10.1103/PhysRevD.111.052003 for the tabulated cross sections and all their individual uncertainties for all covered final states.

[47] Y. I. Azimov, Y. L. Dokshitzer, V. A. Khoze, and S. I. Troyan, Humpbacked QCD plateau in hadron spectra, Z. Phys. C **31,** 213 (1986).

[48] Y. L. Dokshitzer, V. A. Khoze, and S. I. Troian, On the concept of local parton hadron duality, J. Phys. G **17,** 1585 (1991).

[49] D. de Florian, M. Epele, R. Hernandez-Pinto, R. Sassot, and M. Stratmann, Parton-to-kaon fragmentation revisited, Phys. Rev. D **95,** 094019 (2017).

[50] This is in contrast to strange-baryon production, where PYTHIA is found to underestimate hyperon production with increasing strangeness [51].

[51] M. Niiyama *et al.* (Belle Collaboration), Production cross sections of hyperons and charmed baryons from e^+e^- annihilation near $\sqrt{s} = 10.52$ GeV, Phys. Rev. D **97,** 072005 (2018).